

Article

Energy Drive for the Kiruna Mining District Mineral System(s): Insights from U-Pb Zircon Geochronology

Leslie Logan ^{1,*} , Joel B. H. Andersson ¹, Martin J. Whitehouse ², Olof Martinsson ¹ and Tobias E. Bauer ¹

¹ Division of Geosciences and Environmental Engineering, Luleå University of Technology, SE-971 87 Luleå, Sweden; joel.bh.andersson@ltu.se (J.B.H.A.); olof.martinsson@ltu.se (O.M.); tobias.bauer@ltu.se (T.E.B.)

² Department of Geosciences, Swedish Museum of Natural History, SE-104 05 Stockholm, Sweden; martin.whitehouse@nrm.se

* Correspondence: leslie.logan@ltu.se; Tel.: +46-920-491855

Abstract: The Kiruna mining district, Sweden, known for the type locality of Kiruna-type iron oxide–apatite (IOA) deposits, also hosts several Cu-mineralized deposits including iron oxide–copper–gold (IOCG), exhalative stratiform Cu-(Fe-Zn), and structurally controlled to stratabound Cu ± Au. However the relationship between the IOA and Cu-systems has not been contextualized within the regional tectonic evolution. A broader mineral systems approach is taken to assess the timing of energy drive(s) within a regional tectonic framework by conducting U-Pb zircon geochronology on intrusions from areas where Cu-mineralization is spatially proximal. Results unanimously yield U-Pb ages from the early Svecofennian orogeny (ca. 1923–1867 Ma including age uncertainties), except one sample from the Archean basement (2698 ± 3 Ma), indicating that a distinct thermal drive from magmatic activity was prominent for the early orogenic phase. A weighted average ²⁰⁷Pb/²⁰⁶Pb age of 1877 ± 10 Ma of an iron-oxide-enriched gabbroic pluton overlaps in age with the Kiirunavaara IOA deposit and is suggested as a candidate for contributing mafic signatures to the IOA ore. The results leave the role of a late energy drive (and subsequent late Cu-mineralization and/or remobilization) ambiguous, despite evidence showing a late regional magmatic-style hydrothermal alteration is present in the district.

Keywords: Kiruna; mineral system; U-Pb zircon geochronology; IOA; IOCG



Citation: Logan, L.; Andersson, J.B.H.; Whitehouse, M.J.; Martinsson, O.; Bauer, T.E. Energy Drive for the Kiruna Mining District Mineral System(s): Insights from U-Pb Zircon Geochronology. *Minerals* **2022**, *12*, 875. <https://doi.org/10.3390/min12070875>

Academic Editor: Ryan Mathur

Received: 18 May 2022

Accepted: 6 July 2022

Published: 11 July 2022

Publisher's Note: MDPI stays neutral with regard to jurisdictional claims in published maps and institutional affiliations.



Copyright: © 2022 by the authors. Licensee MDPI, Basel, Switzerland. This article is an open access article distributed under the terms and conditions of the Creative Commons Attribution (CC BY) license (<https://creativecommons.org/licenses/by/4.0/>).

1. Introduction

The northern Norrbotten ore province, Sweden, is broadly described as an iron oxide–copper–gold (IOCG) district (cf. [1–5]), and the mining activities related to iron oxide–apatite (IOA) deposits and Cu ± Au mineralization are important for supplying metals to Europe. The large volume of Na-(Ca) alteration (manifested as albite, scapolite, and actinolite) and abundance of low-Ti iron oxide ores (Kiirunavaara, Malmberget) together with structurally controlled hydrothermal Cu ± Au occurrences are shared characteristics with other IOCG districts worldwide [3,6,7]. Despite the growing body of literature on these deposits, the nature and genesis of IOCG deposits and their relationship to IOA deposits are still of major debate. IOA deposits have been suggested to represent the deeper-set roots of an IOCG system where the two deposit styles represent a single evolving magmatic–hydrothermal system (e.g., in the Great Bear Magmatic Zone and the Chilean Iron Belt; [8–11]). On the other hand, the classification of IOA and IOCG as two groups with distinct geneses or as two end members that occur with separate ore-forming components and conditions is preferred [4–7,12]. For example, some authors adopt a purely orthomagmatic genesis for IOA deposits where volatile- and iron-rich melts form from magma immiscibility [13–16], whereas in IOCG deposits, a direct link between magmatic fluids and metal sources for the ore can be ambiguous in some localities (cf. [4]). For example, surface- or basin-derived brines driven by igneous or crustal heat and metamorphic–hydrothermal

fluids have been postulated fluid sources for IOCG-style deposits (cf. [4]), revealing the complications in grouping IOCG and IOA systems under one genetic model.

Due to the large and complicated nature of these ore deposit systems, investigating the possible relation between IOA and IOCG deposits utilizing a broader-scale mineral systems approach can be important for understanding the genetic processes. A mineral systems approach assesses essential ore-forming ingredients on a variety of scales such as energy drive, fluid and metal sources, transport pathways, and traps [17]. However, even if certain mineral system components are shared, if the timing of the two systems is fundamentally distinct, they cannot be attributed to forming from the same hydrothermal system, as emphasized by Groves et al. [6] and Skirrow [7].

An added element of complexity to the mineral systems approach occurs in regions with long and complicated tectonic histories, such as the Norrbotten province, which has experienced several phases of extension and deformation resulting in compound structural patterns and overprinting magmatic and metamorphic events (cf. [2,5,18–22]). Furthermore, the landscape has been shaped by Quaternary glaciation leaving extensive till coverage and poor outcrop exposure. Radiometric age constraints (generally U-Pb zircon and titanite and Re-Os molybdenite) indicate a significant IOA and IOCG mineralization period occurred during the early Svecokarelian (ca. 1880–1860 Ma; [5,23–29]). However, increasing structural and geochronology data link IOCG-style mineralization to a late phase of the tectonic evolution (ca. 1.82–1.78 Ga; [5,18–21,27]). These data raise an important question about the timing of introduction and/or remobilization of Cu ± Au when assessing the genetic relationship between IOA and IOCG systems in Norrbotten.

In this study, the energy drive of the Kiruna mining district mineral systems is investigated. Energy drives can include, for example, metamorphic or magmatic events, or sedimentary thickness [30]. Metamorphic events correlating to the Svecokarelian orogeny in Norrbotten have been dated by several authors (cf. [31] and references therein), however, ages related to the early Svecokarelian metamorphic event are rare in literature [25,32], with results more often yielding late orogenic or younger ages (cf. [31] and reference therein, [33]). In the Kiruna mining district, structural evidence suggests the area was at a higher crustal level and too shallow to develop ductile fabrics during the early Svecokarelian [21]. Moreover, metamorphic fingerprints from the early (M_1) phase are either absent, masked, or unidentified (cf. [21]). Consequently, this study focuses on the absolute timing of magmatic intrusions as a more robust way to elucidate the timing of energy driving processes. Both the early and late Svecokarelian orogenic phases overlap with magmatic events and highly saline fluids affected the district rocks and local ore deposits, interpreted to reflect mobilized evaporite components from elevated heat and fluid flow from magmatism [5,26,34–37]. The samples collected for the study were taken from an area situated 5 km south of the giant Kiirunavaara IOA deposit in spatial proximity to the Rakkurijärvi (IOCG-style) deposit and Pahtohavare epigenetic Cu (Fe-Au) deposits. Importantly, while the Rakkurijärvi deposit has been constrained radiometrically to the early Svecokarelian mineralizing period (Re-Os molybdenite, U-Pb allanite, rutile; [5,26,27]), the age of the Pahtohavare deposits is unknown. However, previous studies have found evidence for a partial contribution of magmatic fluids on the ore formation at both localities studied (fluid inclusions [5,34,36,37], Cl/Br ratios and $\delta^{37}\text{Cl}$ on scapolite [38], C and O isotopes on carbonate [26], Sm-Nd on titanite [39]), indicating the magmatism likely served as an energy driver and possibly a metal and fluid supplier for the mineral systems.

The focus of most geochronology studies in the Kiruna mining district has been on the plutonic and volcanic rocks within the vicinity of the Kiirunavaara IOA deposit, which has indicated a dominance of early Svecokarelian igneous activity [23,24,28]. One study [24], however, showed that a late Svecokarelian intrusion (U-Pb ICP-MS on zircon and titanite) occurs approximately 10 km southwest of Kiirunavaara implying that both regional magmatic events affected the Kiruna mining district. With two overprinting magmatic episodes potentially driving two time-separated mineral systems in Kiruna, it is important to illuminate the ages of the plutonic activity to holistically understand the

timing of ore formation/remobilization. The samples taken for this study are representative of the intrusive bodies exposed at the current erosional level in Kiruna. Although they are from a relatively small sampling area, the data from this study taken with previous geochronological results contribute to the understanding of IOA and IOCG mineral systems and are placed into context of the regional tectonic framework.

2. Geological Setting

The nomenclature of the rocks used in this paper follows that described by Martinsson [40] where the “meta” prefix is excluded for clarity and emphasis on the original protolith (as all rocks are variably metamorphosed to greenschist or lower amphibolite facies).

2.1. Regional Geologic Setting

The underlying basement rocks of the Norrbotten craton are exposed just north of Kiruna in the Norrbotten province (Figure 1) and consist of Neo-Archean (ca. 2.9–2.6 Ga) gneissic granitoids of tonalitic to granodioritic composition, amphibolites, and paragneisses [2,41] formed from continental buildup during the Lopian orogeny [2]. During the early Paleoproterozoic, rifting of the basement (ca. 2.5–2.0 Ga) generated a prominent greenstone belt of tholeiitic volcanic and volcanoclastic rocks, and rift-related sedimentary successions [42–45] spanning from Norway to Russia Karelia [43].

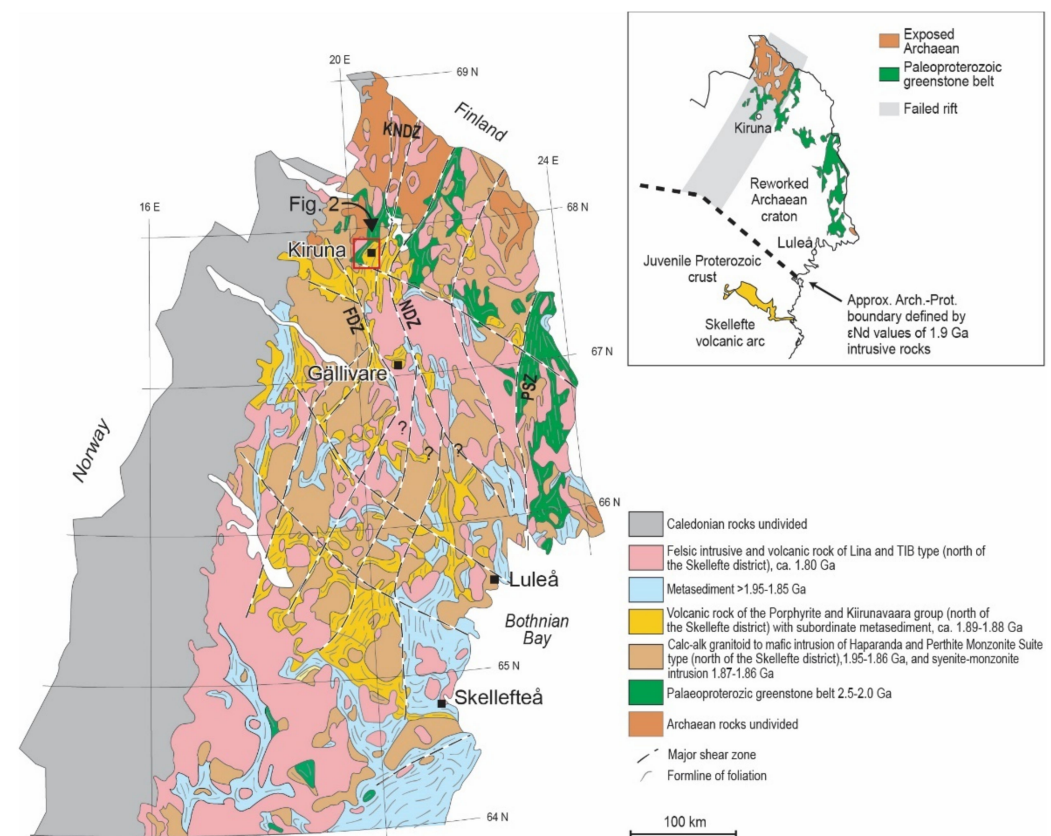


Figure 1. Geologic map of northern Sweden including the Skellefte district and northern Norrbotten ore province. Inset shows approximate location of the paleoboundary of the Archean craton [46]. FDZ = Fjällåsen deformation zone, KNDZ = Kiruna–Naimakka deformation zone, NDZ = Nautanen deformation zone, PSZ = Pajala shear zone. Modified after Bauer et al. [19], Weiheid and Williams [47], and Bauer and Andersson [48].

A shift from rifting and basin development to a subduction system marked the beginning of the polyphase Svecokarelian accretionary orogenic cycle (ca. 1.90–1.78 Ga) with related arc and back-arc magmatism [2]. Approximately three to four successive mid- to

late-Paleoproterozoic deformation events (described below) are recorded in the Norrbotten lithotectonic unit and have been constrained by ages of magmatic rocks, hydrothermal alteration, and structural characterization (cf. [2] and references therein; [5,18–21,49,50]).

2.1.1. Extension and Early Orogenic Crustal Shortening

At ca. 1.90 Ga, early NE-directed subduction and back-arc extension in northern Norrbotten commenced, followed by the accretion of the Skellefte volcanic arc in the south onto the Archean craton to the north (termed D_1 in Norrbotten, but D_2 in the Skellefte district and Överkalix lithotectonic unit; Figure 1, [31,46,51,52]). Recent geochronological–structural investigations have shown that the timing of early back-arc extension, volcanism, and associated synvolcanic faulting can be bracketed within 1887 ± 3 Ma (syn-basin deposition volcanic, U-Pb zircon; [22]) to a least ca. 1874 ± 9 Ma in the Kiruna area (age of the hanging wall of the Rektor deposit, U-Pb zircon; [28]). The igneous intrusive–extrusive suites associated to this early period of the Svecokarelian orogeny include the co-magmatic, calc-alkaline to alkali-calcic, synorogenic Haparanda suite–Porphyrite group and Perthite monzonite suite (PMS)–Kiirunavaara group [2]. Radiometric dating (U-Pb zircon) of these units indicate intrusion from ca. 1.89–1.86 Ga, with the Haparanda suite magmatism and Porphyrite group volcanics occurring slightly earlier (with overlap) than the PMS–Kiirunavaara group rocks [2]. Furthermore, Haparanda suite–Porphyrite group rocks are generally predominant in the eastern part of the Norrbotten province while the PMS–Kiirunavaara group rocks dominate in the west. Early district-scale Na-Ca metasomatism occurred during this period with the formation of albite, marialitic scapolite, magnetite, amphibole, and carbonate [2,5,20,35].

Subsequent crustal shortening (D_1) formed a penetrative tectonic fabric from an inferred NE–SW shortening direction [18–21,49,50]. The fabric development overlapped with peak metamorphic conditions (lower amphibolite) recorded by syntectonic growth of hornblende [20]. Regionally, amphibolite facies metamorphism is associated to D_1 , but in the Kiruna mining district the metamorphism is of upper greenschist facies.

2.1.2. Late Orogenic Crustal Shortening

The second phase of the Svecokarelian orogeny (D_2 ; ca. 1.82–1.78 Ga) is characterized by E–W crustal shortening and basin inversion as recorded in the central Kiruna area [21]. The deformation is associated with brittle–plastic conditions producing spaced S_2 cleavages and strong strain partitioning [18,20], in contrast to the mostly plastic conditions of D_1 . The timing of the late orogenic period is broadly constrained to ca. 1.82–1.78 Ga from radiometric ages from metamorphic minerals and plutonic rocks and by using cross-cutting relationships of tectonic fabrics with known plutonic ages [2,20,32,33,53]. However, a direct geochronological constraint on deformation has recently been obtained on syntectonic titanite (U-Pb LA-ICP-MS) approximately 5 km east of the Kiruna district, which indicates the hosting shear zone was active around 1812 Ma during an event lasting up to 20 m.y. [22].

Widespread anatectic S-type, silica-rich granites of the Lina suite [2,53,54] and quartz-poor monzonitic A-/I-type granitoids, syenites, and gabbros of the Transscandinavian Igneous Belt (TIB, e.g., Edefors suite) intruded in northern Sweden during D_2 [32,53,55,56]. The associated metamorphic conditions have been suggested to be of high temperature, low pressure characteristics related to the abundant magmatism [2,18]. Commonly, a potassic–ferroan alteration is associated to D_2 structures in Norrbotten [19,20]. For example, calcic and potassic–ferroan metasomatism is observed in late orogenic structures in the Nautanen deformation zone with the assemblage K-feldspar–quartz–biotite–amphibole–magnetite–hematite–epidote–scapolite–sulfide commonly spatially associated to syn- D_2 granitoids and pegmatites [18,19]. However, K-bearing alteration is also observed related to early Svecokarelian ore-forming events (e.g., Rakkurijärvi, Per Geijer iron ores; [5,26]). In addition, radiometric dating suggests that a late sodic–calcic alteration style also developed during D_2 [22], implying that the hydrothermal alteration associated to the early- and

late-cycle tectonomagmatic events in Norrbotten was of similar character, complicating the usage of mineral parageneses as vectors toward specific ore deposits.

The latest structures recorded in Norrbotten reflect the last stages of the Svecokarelian orogeny and the transition into a post-orogenic collapse [19,21]. A D_3 event records a clockwise-rotation of the stress field into a NNW–SSE- to N–S-orientation with crustal shortening that resulted in a gentle refolding of pre-existing fabrics and crenulation of white mica and chlorite domains [21]. The fourth event is brittle in nature and cuts earlier fabrics [21]. An example includes a late calcite–quartz hydraulic brecciation at the Luossavaara and Rektor IOA deposits that cross-cuts an S_2 fabric [21]. Additionally, hydrothermal U–Pb monazite ages from the Rektor and Kiirunavaara deposits [57,58] and U–Pb ages of stilbite, titanite, and apatite from open fractures at the Malmberget deposit [59] indicate two disturbance events at ca. 1.74 Ga and 1.62 Ga that are possibly coeval with the hydraulic fracturing and constrains the latest tectonothermal events identified so far in northern Norrbotten.

2.2. Local Geology

2.2.1. Stratigraphy and Local Intrusive Rocks

The stratigraphy in the Kiruna area, here called the Kiruna mining district (defined by Figure 2), is composed of well-preserved rocks and comprehensive overviews of the stratigraphy have been made by Lundbohm [60], Frietsch [61], Bergman et al. [2], Martinsson et al. [5], and Andersson et al. [21].

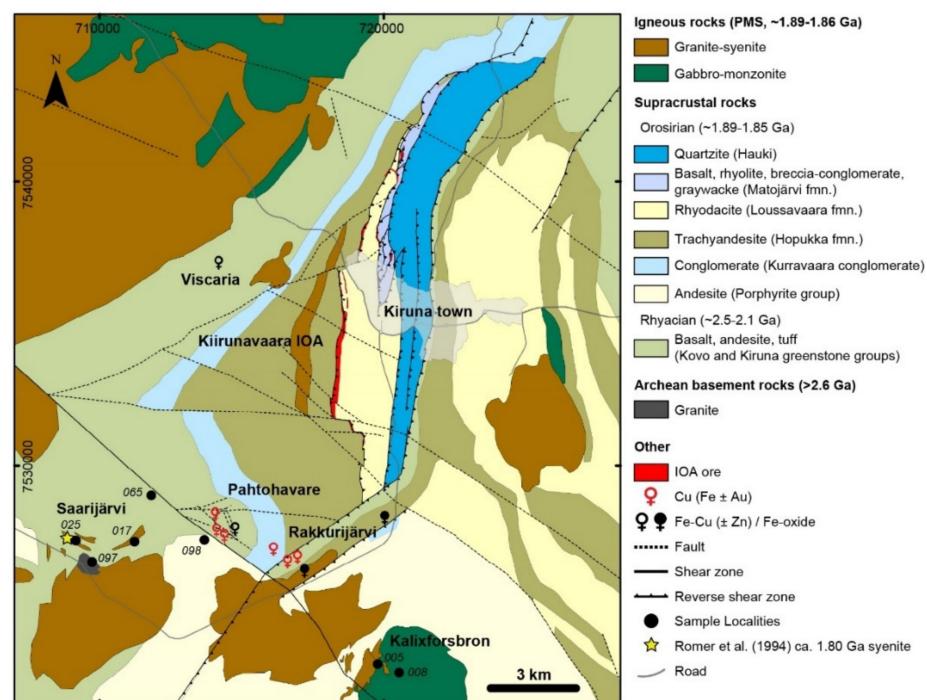


Figure 2. Geologic map of the Kiruna mining district showing stratigraphy, structures, and igneous intrusions. Kiruna town is marked in gray. Sampling locations and the local names of the areas are indicated. Modified after Martinsson et al. [62] and Andersson et al. [21]. Coordinate system in SWEREF99.

In the Kiruna mining district (Figure 2) the stratigraphic units young to the east. The lowermost units unconformably overlie the Archean basement and belong to the Kovo group, deposited during the earliest episodic rifting period in the Paleoproterozoic (ca. 2.5–2.3 Ga, [43]). The Kovo group is a 1–2 km thick package [41] of conglomeritic and volcanoclastic rocks, tholeiitic lavas, and calc-alkaline mafic to intermediate volcanics [43]. The best-preserved stratigraphy of this rock succession outcrops north of Kiruna in the Kovo area. Overlying the Kovo group is the Kiruna greenstone group, which hosts the Viscaria

and Pahtohavare syngenetic and epigenetic Cu (\pm Au \pm Fe \pm Zn) deposits [43]. The Kiruna greenstone group consists of a series of basaltic lavas, conglomerates, and dolostones at the base with overlying successions of komatiitic to tholeiitic volcanics, calc-alkaline volcanosedimentary formations, thin layers of graphitic schists, and pillow basalts. These greenstones are also intruded by mafic sills related to the upper pillow basalt subunit [43].

The Rhyacian Kiruna greenstone group is unconformably overlain by the mid-Orosirian Kurravaara conglomerate, a polymictic, poorly sorted conglomerate composed of rounded to subrounded clasts of approximately 0.5 to >10 cm (locally up to 50 cm) in size [61] (Figure 2). The Kurravaara conglomerate is overlain by trachyandesitic volcanic rocks of the Hopukka formation that make up the footwall of the Kiirunavaara IOA deposit. The hanging wall to the deposit consists of dacitic–rhyolitic volcanic rocks of the Luossavaara formation (ca. 1890–1874 Ma) [23,28,40,63]. The Luossavaara formation is overlain by units of rhyolitic tuffs, basaltic lavas, breccia conglomerates, and graywackes of the Matojärvi formation [40]. Finally, these formations are overlain by the Hauki quartzite, composed of arenites and quartz–arenites that display well-preserved cross-bedding, and breccia–conglomerates. The unit represents the youngest rocks of the stratigraphy. The eastern boundary of the Hauki quartzite marks a tectonic repetition where a greenstone unit is juxtaposed next to the Hauki quartzite [64].

Both regionally and locally, the designation of Svecokarelian intrusions to a specific time period has been made based on the foliation development and chemistry (e.g., foliated calc-alkaline Haparanda suite versus weakly foliated alkali–calcic PMS), mineralogy (e.g., less mafic minerals belonging to Lina suite equivalents), or with magnetic field patterns [2]. However, these methods may result in misleading classifications where strain partitioning is prevalent and where mineralogical compositions overlap between igneous suites. Geochronological investigations have been carried out on the intrusive bodies in direct vicinity to the IOA deposits in the central Kiruna area [23,24,28], but are sparse in other parts of the Kiruna mining district, such as in the south where the Pahtohavare and Rakkurijärvi deposits occur in spatial proximity to igneous intrusions (Figure 2). Currently, most intrusions are classified as PMS suite and are suggested to represent the deeper magma chambers that produced the Kiirunavaara group volcanic rocks that host the IOA deposits [40,65]. In the southern part of the district, only one intrusion has been dated (1792 ± 4 Ma, U–Pb inductively coupled plasma mass spectrometry (ICP–MS) intercept age from zircon and titanite fractions; Figure 2; [24]) and is the only known igneous body of ca. 1.80 Ga (D_2) age in the area. For a summary of geochronology data on the plutonic and volcanic rocks in the Kiruna mining district, see Figure 3.

2.2.2. Ore Deposits and Alteration

A variety of ore deposit types are present in the Kiruna mining district including the Kiirunavaara and other IOA deposits, stratiform–stratabound Cu (Fe–Zn) deposits (i.e., Viscaria, Eastern Pahtohavare), epigenetic Cu \pm Au deposits (Pahtohavare), and IOCG-style deposits (Rakkurijärvi; [26,43]). Of these deposit types, the IOA, the Pahtohavare epigenetic Cu \pm Au, and the Rakkurijärvi IOCG deposits are interpreted to have formed during the Svecokarelian orogeny (ca. 1.90–1.78 Ga, cf. [5,26,28]).

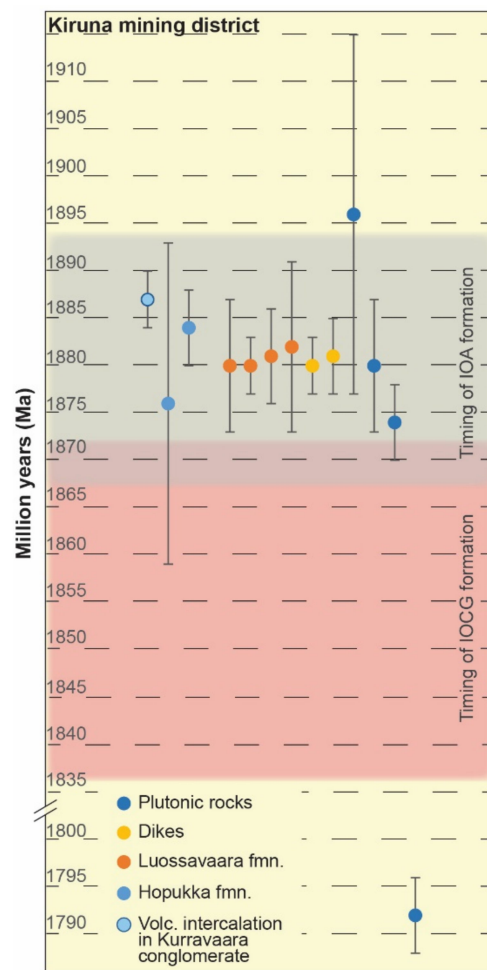


Figure 3. Summary of U-Pb (ICP-MS and SIMS zircon and titanite) geochronology data on volcanic-plutonic rocks in the Kiruna mining district. Gray and red shadows mark approximate time boundaries of IOA and IOCG formation in the Kiruna mining district, respectively. Data from [5,22–24,26–28,66].

The Kiirunavaara and other IOA deposits (Figure 2) in the Kiruna mining district have been studied for over a century. The Kiirunavaara deposit occurs within the Kiirunavaara group volcanics as a tabular low-Ti magnetite–apatite orebody with magnetite–actinolite ore-breccias developed at both the hanging wall and footwall contacts [2]. Albitization occurs in the footwall and varying amounts of actinolite, albite, biotite, and scapolite occur as common alteration minerals around the deposit [2,5]. Various hypotheses about the genesis of the Kiirunavaara deposit include magmatic intrusive [67–69] to extrusive [13,70] to sedimentary–exhalative [71], and hydrothermal [72]. The timing of IOA formation in Kiruna has been constrained by radiometric dating of both host rocks and associated alteration and ore minerals [5,23,24,27,63], which illuminates the close temporal relation of the PMS–Kiirunavaara group and the IOA deposits. The closest direct age determination has been done by Westhues et al. [28] on zircon grains extracted directly from the Kiirunavaara and Nukutus magnetite ores that yielded ages of 1874 ± 7 Ma and 1877 ± 4 (U-Pb secondary ion mass spectrometry (SIMS)), respectively, which overlap with a titanite age from a decimeter-wide calc-silicate alteration zone at the footwall contact to Kiirunavaara (1878 ± 4 Ma, U-Pb thermal ion mass spectrometry (TIMS); [5]).

The Rakkurijärvi IOCG ores occur approximately 5 km SSE of the Kiirunavaara IOA (Figure 2) and are hosted in the Kurravaara conglomerate and Kiirunavaara group volcanics. Rakkurijärvi is described as an IOCG deposit with the ore occurring primarily in a range of sulfide-mineralized breccia styles [26]. The host rocks are brecciated to varying degrees and the main mineralization occurs as magnetite breccias with chalcopyrite–calcite

matrix infill. Additionally, within the Kurravaara conglomerate Cu mineralization occurs and selective–pervasive magnetite replacement of conglomerate clasts suggests some mineralization to be a result of hydrothermal replacement [26]. Na–Ca–Fe alteration (albite–scapolite–actinolite–magnetite) accompanied the early magnetite precipitation in the rocks, which was overprinted by K-alteration (K-feldspar–scapolite–biotite) and a later low-temperature epidote–hematite–muscovite–chlorite assemblage [26]. C and O isotopes of calcite from veins, breccia matrices, and marble indicate that the Rakkurijärvi ore-related calcite derived isotopic signatures from both magmatic and marine carbonate sources [26]. Furthermore, ϵNd isotope data from titanite at Rakkurijärvi indicate an overlap with the regional values for granitoids from the early Svecokarelian [26,39]. The deposit is dated by Re–Os (molybdenite: 1862 ± 6 Ma and 1853 ± 6 Ma) and U–Pb (laser ablation (LA)–ICP–MS on allanite: 1854 ± 18 Ma, and TIMS on rutile: 1859 ± 2 Ma) constraining the timing of formation to ca. 1.86 Ga [5,26,27], toward the end of the early Svecokarelian cycle (late D₁) in northern Norrbotten.

The deposits at Pahtohavare are situated approximately 5 km SW of the Kiirunavaara IOA deposit (Figure 2) and are hosted in mafic to intermediate tuffites, mafic sills, and graphite schist horizons of the Kiruna greenstone group. One ore body is interpreted to be syngenetic and to have formed with the deposition of the greenstones, whereas three deposits are described as epigenetic [73]. The epigenetic ores are structurally and lithologically controlled and have previously been suggested to be of similar age as the Rakkurijärvi deposit [5]; however, no direct age determination has been carried out. The mineralization assemblage consists of pyrite and chalcopyrite occurring disseminated and as breccia infill in pervasively albite-altered graphite schist and tuffite horizons. Additionally, pyrite and chalcopyrite occur in quartz–carbonate (calcite and ferrodolomite) veins. Thin magnetite-rich horizons occur within the hosting tuffites [34,73]. Fluid inclusion studies indicate a highly saline and hot (>500 °C) fluid was responsible for early quartz and pyrite vein precipitation [34], with Cl/Br ratios on fluid inclusion leachates reflecting mixed magmatic–hydrothermal and evaporitic fluid sources [37]. Cu contents in hypersaline brines from Pahtohavare range from ~100–500 ppm and have been compared to saline magmatic fluids from the Cloncurry District, Australia [37]. Furthermore, Cl/Br ratios and $\delta^{37}\text{Cl}$ isotope signatures of marialitic scapolite from scapolite-altered host rocks near the Pahtohavare deposit records mixed magmatic and residual brine/halite signatures [38]. Together, both direct and indirect evidence suggest that magmatic fluids were involved in the formation of scapolite alteration and mineralizing veins at Pahtohavare.

3. Materials and Methods

3.1. Geologic Sampling

Sampling was conducted both in the field and at the Geological Survey of Sweden's National Drill Core Archive in Malå during 2019. Samples for geochronology were taken as fresh specimens from outcrops for analysis. Thin sections for microscopic investigations were prepared by Precision Petrographics Ltd. in Vancouver, Canada, for microscopic investigation. See Table 1 for additional sample information.

Table 1. Sample information.

Sample Name	Alias	Association	Relative Timing	Description	Location	SWEREF99 TM		Age (Ma, This Study)
JBHA19005	005	PMS	Early orogenic	Aplitic granite	Kalixforsbron	N 7523019	E 719786	Early orogenic
JBHA19008	008	PMS	Early orogenic	Magnetite–ilmenite gabbro	Kalixforsbron	N 7522725	E 720539	1877 ± 10
JBHA19017	017	PMS	Early orogenic	Granite	Saarijärvi	N 7527323	E 711237	1887 ± 4
JBHA19025	025	PMS	Early orogenic (Late orogenic in [24])	Quartz syenite	Saarijärvi	N 7527359	E 709173	1880 ± 7
LLPAH19065 (Drill hole PAH92002, 19 m)	065	PMS	Early orogenic	Granite	Saarijärvi	N 7528947	E 711824	1880 ± 3
LLSAR19097	097	Neoproterozoic Porphyrite group?	Archean	Granite	Saarijärvi	N 7526604	E 709743	2698 ± 3
LLPAH19098	098		Early orogenic	Porphyritic quartz andesite	Pahtohavare	N 7527381	E 713693	1911 ± 12

3.2. Lithochemistry

Samples were crushed and powdered following conventional methods at ALS Minerals in Piteå, Sweden. Lithochemical total whole rock characterization data were obtained from Bureau Veritas Laboratories, Vancouver, Canada. Major elements and oxide concentrations were determined through lithium borate fusion dissolution coupled with ICP–atomic emission spectroscopy analysis, whereas trace elements (including rare earth elements (REE)) were measured with ICP–MS. Complementary elements (Mo, Cu, Pb, Zn, Ni, As, Cd, Sb, Bi, Ag, Au, Hg, Tl, Se) were processed by digesting the sample with a modified aqua regia solution (1:1:1 HNO₃:HCl:H₂O) and measured by inductively coupled plasma (ICP)–emission spectroscopy (ES) or mass spectroscopy (MS) analysis. FeO speciation was determined separately by titration. QA/QC was carried out by submitting blind duplicates and certified standards from the United States Geological Survey (AVG-2 and GSP-2) to assess reproducibility and accuracy, respectively.

3.3. U–Pb Zircon Geochronology

Samples were mechanically reduced to a grain size of ≤ 1.3 mm using a tabletop digital BB-50 Fritsch jaw crusher and an agate mill. Both the jaw crusher and the mill were subjected to a strict cleaning protocol. Heavy mineral concentrates were obtained from a 70–90 µm fraction via a hydroseparation system at Luleå University of Technology (LTU) through a two-step series. A computer-controlled CNT HS 11 device [74] pulsed water from a high potential energy source firstly through a 30 cm glass separation (J-shaped) tube to prepare a pre-concentrate. The pre-concentrate was pulsed through a 10 cm glass separation tube to obtain a final concentrate. Heavy minerals were panned in a watch glass and picked under water aided by a binocular microscope. For magnetic samples, magnetic minerals were removed in advance using a hand magnet and a Frantz Isodynamic Magnetic Separator. Zircon grains were mounted in epoxy resin with the Geostandards 91500 (²⁰⁷Pb/²⁰⁶Pb age of 1065 Ma, ²⁰⁶Pb/²³⁸U age of 1062 Ma; [75]) and the M257 zircon reference material (²⁰⁶Pb/²³⁸U age of 561.3 ± 0.3 Ma; [76]), polished, and imaged by scanning electron microscopy (SEM) for both backscatter electron (BSE) and cathodoluminescence (CL) images. Post-analysis BSE and CL imaging was also undertaken to assess the spot locations.

Samples were gold-coated and analyzed at the NordSIMS Laboratory at the Swedish Museum of Natural History using a CAMECA IMS 1280 ion microprobe. A 10 nA oxygen primary beam was generated using an Oregon Physics Hyperion H201 high-brightness, radiofrequency plasma source and focused in Gaussian mode onto the sample in approximately a 15 µm spot diameter (a 5 µm raster was retained during analysis to homogenize the focused beam over a larger area). A single ion counting electron multiplier measured the secondary ions in the mass spectrometer over 10 cycles of data. Details of the analytical procedure and calibration strategy closely follow those outlined by Whitehouse and Kamber [77] and Jeon and Whitehouse [78]. The ²⁰⁶Pb/²³⁸U ratios were calibrated using the zircon Geostandards 91500, with the session reproducibility propagated in quadrature

onto the individual run uncertainties, along with an additional 0.5% uncertainty to take account of the slight discordance reported from 91500 [75]. Given the very high stability of the RF plasma primary beam and consequently restricted range in UO_2/U ratio compared to duoplasmatron sessions, a one-dimensional calibration scheme in which $\text{Pb}/\text{U} = k \times \text{Pb}/\text{UO}_2$ [79] was utilized, with k derived from the average of the 91500 analyses in each session. The $^{207}\text{Pb}/^{206}\text{Pb}$ ratios require no calibration due to the inherently small mass bias at high mass [80] that is well within analytical uncertainty on this ratio. Quality control was monitored using regularly interspersed analyses of the secondary standard M257, which yielded Pb/U ages within 1% of the accepted value from each of the three analytical sessions relevant to this study (Table S1). All data were reduced using in-house software and common Pb corrections were made following the Stacey and Kramers [81] model for terrestrial present-day ^{204}Pb composition. Corrections were made on analyses where the ^{204}Pb count proved statistically significant compared to the session average detector baseline [82]. U-Pb isotopic data were reduced using the Excel Isoplot add-in [83]. Decay constants follow the recommendations of Steiger and Jäger [84].

4. Results

4.1. Sample Descriptions

4.1.1. Kalixforsbron Area—Samples 005, 008

Sample 005 was collected from a granitic outcrop adjacent to a large gabbroic pluton in the Kalixforsbron area (Figure 2). The granite is fine-grained with a sugary texture (Figure 4a), and in thin section, the sample is hypidiomorphic with subequal quantities of quartz, plagioclase, and feldspar, and minor biotite, chlorite, and muscovite. Accessory minerals include zircon and apatite. Grain boundaries of quartz and feldspar crystals are serrated, and quartz shows bulging recrystallization textures (Figure 4b). The contact zone between the granite and the gabbroic pluton is characterized by hydraulic breccias associated with K-feldspar + quartz + epidote potassic alteration affecting gabbroic rocks within a structure showing both plastic and brittle deformation (Figure 4c). The zircon grains for sample 005 are pink, weakly prismatic or subhedral, and show oscillatory to irregular zonation patterns and occasional resorption embayments (Figure 4d). Many zircon grains are highly fractured with textures showing rehealed fracture planes and these areas were avoided for the analyses. Several zircon grains show an inclusion-rich “spongy” oscillatory growth zone toward the edge of the grains.

Sample 008 is a magnetite–ilmenite gabbro (Figure 4e) from within the gabbroic pluton (Figure 2). In thin section, the sample shows a weak foliation fabric of subhedral to anhedral grains of intermediate plagioclase and clinopyroxene of approximately equal proportions (Figure 4f), and interstitial magnetite–ilmenite (15%–20% modal abundance). Magnetite inclusions can be found in clinopyroxene and plagioclase. Fine-grained reaction coronas occur between magnetite–ilmenite and plagioclase grains (Figure 4f). Ilmenite exsolutions occur in magnetite, and apatite is abundant in the sample (Figure 4f). Seven zircon grains were collected from 5 kg of sample. These were transparent and subhedral to rounded, oscillatory zoned, and with rims that show a very bright CL signal (Figure 4g).

4.1.2. Saarijärvi Area—Samples 017, 025, 065, 097

Sample 017 from the Saarijärvi area (Figure 2) was sampled from a strongly magnetic (magnetite-bearing), medium-fine-grained granitic rock rich in potassium feldspar, with patchy areas of coarse quartz–potassium feldspar alteration (Figure 5a). Optical microscopy reveals hypidiomorphic equigranular with myrmekitic to granophyric textures of quartz and albite occurring interstitially between feldspar grains and as grain boundary replacement textures (Figure 5b). K-feldspar replaces plagioclase grains in patchy textures. Zircon grains from the sample are pink and have narrow prismatic, broad prismatic, and stubby shapes (Figure 5c). Internal textures are generally homogenous with limited irregular to concentric internal zonation. The zircon grains have a moderate crack density and are often broken (Figure 5c).

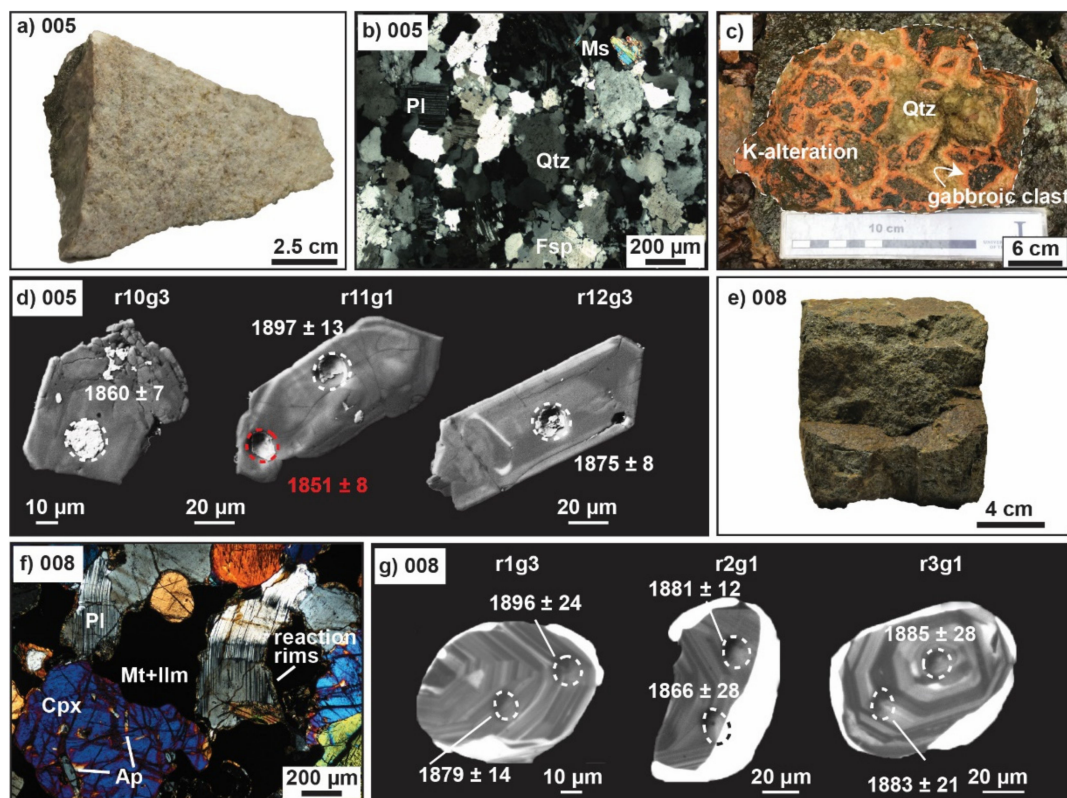


Figure 4. Sample images from the Kalixforsbron area. (a) Hand specimen for sample 005 showing fine-grained granitic texture. (b) Micrograph in cross-polarized light (XPL) of sample 005 with serrated and embayed grain boundaries between quartz, plagioclase, and feldspar. (c) Brecciated and potassic-altered gabbro with quartz infill in a deformation zone at the edge of the gabbroic pluton. (d) Cathodoluminescence images of typical zircon grains for sample 005. (e) Hand specimen of magnetite-ilmenite gabbro. (f) Micrograph of sample 008 magnetite-ilmenite gabbro in XPL with reaction coronas between plagioclase and magnetite-ilmenite. (g) Cathodoluminescence images of typical zircon grains for sample 008. In (d,g), dashed white and black circles highlight each concordant SIMS spot analysis while red circles and text are discordant. Ages reported are $^{207}\text{Pb}/^{206}\text{Pb} \pm 2\sigma$. Abbreviations: Ap—apatite, Cpx—clinopyroxene, Fsp—alkali feldspar, Ilm—ilmenite, Ms—muscovite, Mt—magnetite, Pl—plagioclase, Qtz—quartz.

Sample 025 was collected from a pink, potassic-altered, medium-coarse-grained syenite outcrop (Figure 5d) in the Saarijärvi area close to the locality previously dated to be 1792 ± 4 Ma (syenite from drill core; U-Pb ICP-MS intercept age from zircon and titanite fractions) by Romer et al. [24] (Figure 2), and is the only known intrusion of late orogenic age in the district. The sample in thin section shows a relict hypidiomorphic equigranular texture of mostly alkali feldspar and minor quartz, with serrated to lobate grain boundaries between alkali feldspar grains and partial conversion to a fine-grained mineral phase along cleavage planes and cracks (Figure 5e). The sample has brittle fractures filled with chlorite, rutile, and titanite. The zircon grains from the sample are transparent or with tints of yellow, orange, and red. They are prismatic with the majority showing complex zoning patterns and few showing oscillatory zoning (Figure 5f). Resorbed textures indicate multiple generations of zircon stability which were targeted in the radiometric analysis. Fracture density is moderate, and it is common to see radial fractures around cores that are dark in CL imagery, suggesting high-U cores and differential volume expansion during metamictization [85,86].

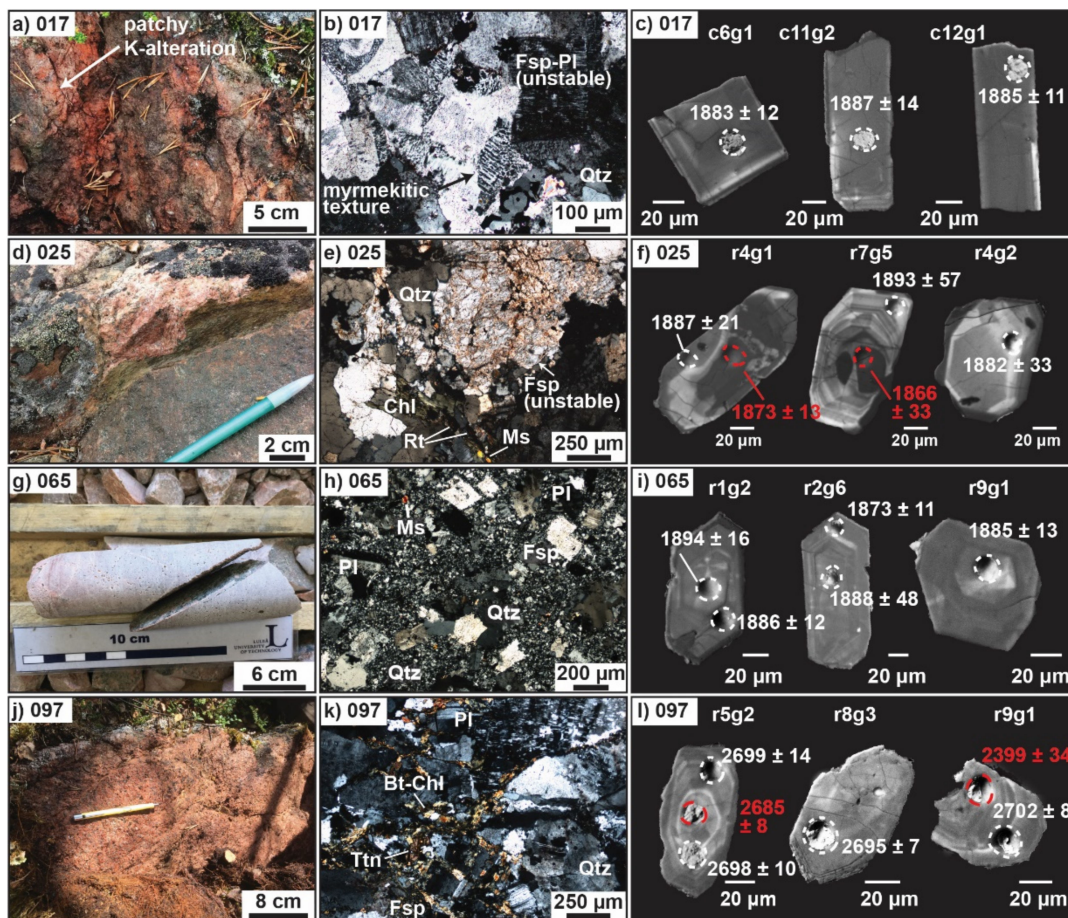


Figure 5. Sample images from the Saarijärvi area. (a) Outcrop at the sampling locality 017 showing patchy K-feldspar alteration with quartz. (b) Micrograph of 017 showing unstable feldspars and plagioclase with myrmekitic textures along grain boundaries, in XPL. (c) Cathodoluminescence images of typical zircon grains for sample 017. (d) Sample 025, medium-coarse-grained syenite in outcrop with a cross-cutting epidote-altered fracture plane. (e) Micrograph of sample 025 with brittle fractures filled with chlorite, rutile, and muscovite, in XPL. (f) Cathodoluminescence images of typical zircon grains for sample 025. (g) Drill core sample 065 of fine-grained granite intersection. (h) Micrograph of sample 065 showing a porphyritic texture with recrystallized quartz–plagioclase matrix, in XPL. (i) Cathodoluminescence images of typical zircon grains for sample 065. (j) Sample 097, Archean granite in outcrop. (k) Micrograph of sample 097 showing brittle fractures filled with biotite–chlorite, titanite, and feldspar, in XPL; (l) Cathodoluminescence images of typical zircon grains for sample 097. In (c,f,i,l), dashed white circles highlight each concordant SIMS spot analysis while red circles and text are discordant. Ages reported are $^{207}\text{Pb}/^{206}\text{Pb} \pm 2\sigma$. Abbreviations: Bt—biotite, Chl—chlorite, Fsp—alkali feldspar, Ms—muscovite, Pl—plagioclase, Qtz—quartz, Rt—rutile, Ttn—titanite.

Sample 065 was taken from an intersection of fine-grained light pink granitic rock in drill core (Figure 5g), drilled north of Saarijärvi, at approximately 19 m depth (Figure 2). The granitic intersection is approximately 25 m long and has fine veinlets of actinolite, biotite, and quartz with faint red alteration halos. In thin section, the sample has a porphyritic texture with 100–200 μm alkali feldspar and plagioclase laths surrounded by a matrix of fine-recrystallized quartz and fine-grained feldspar (Figure 5h). The zircon grains from sample 065 are orange to pink and are regular prismatic to subhedral prismatic with a moderate fracture frequency. The grains show weak oscillatory zoning, sector zoning, and typically have a thin dark and partially digested rim of $<10 \mu\text{m}$ (Figure 5i).

Sample 097 was collected from a medium-grained quartz-rich granitic rock (Figure 5j) to the south of Saarijärvi (Figure 2) that yielded an Archean age (2710 ± 4 Ma) in a previous study [87]. The sample shows strong deformation textures in quartz and feldspars, based on irregular extinction patterns, embayed to lobate grain boundaries, and quartz bulging quartz recrystallization textures. The sample is highly fractured with infill of biotite–chlorite, feldspar, and titanite (Figure 5k). Zircon grains from the sample have gray and pink coloration, prismatic shapes, and moderate crack density. CL and BSE imagery indicates that a range between homogenous (lacking zones) to oscillatory zonation occurs within the grains, with some grains showing thin (1–5 μm) overgrowth rims that tend to be inclusion-rich (Figure 5l).

4.1.3. Pahtohavare Area—Sample 098

Sample 098 is a porphyritic quartz–andesite (based on modal composition in thin section) with cm-scale plagioclase laths encompassed by a fine-grained biotite-rich matrix (Figure 6). It was sampled ca. 300 m SW of Pahtohavare on the south side of the NW–SE trending shear zone (Figure 2). In outcrop, the fabric varies from randomly oriented laths to small zones of fluidal texture (Figure 6a). In thin section, rounded and slightly deformed masses of quartz with biotite and minor scapolite, epidote, magnetite, and muscovite are interpreted to be relict amygdales. The coarse porphyritic grains of plagioclase are situated within a spaced and unevenly developed fabric defined by biotite. Epidote and fine scapolite porphyroblasts (100–300 μm) occur. Plagioclase grains show minor alteration to epidote, white mica, biotite, and fine-grained magnetite (Figure 6b). Zircon grains for sample 098 from Pahtohavare are transparent and prismatic with oscillatory zones (Figure 6c). Some grains occasionally record an inner zone of inclusions. Weak radial fracture patterns are occasionally observed around cores.

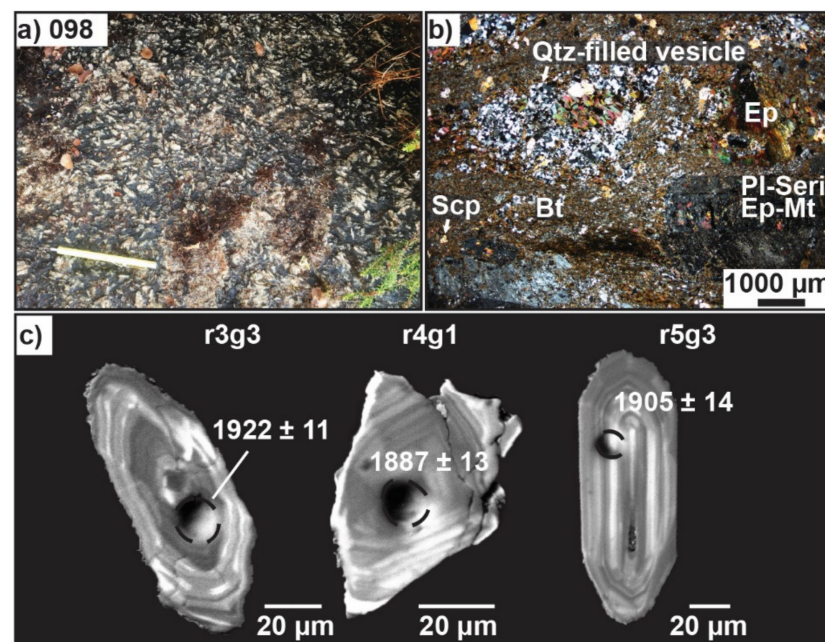


Figure 6. Sample images from the Pahtohavare area. (a) Sample 098 in outcrop showing large plagioclase laths in a fine-grained biotite-rich matrix. Mineral orientation varies from unoriented to oriented. (b) Micrograph in XPL of sample 098 porphyritic texture with large plagioclase laths converting into white mica–epidote–magnetite. Scapolite porphyroblasts occur in the biotite-rich matrix. (c) Cathodoluminescence images of typical zircon grains for sample 098. Dashed white and black circles highlight each concordant SIMS spot analysis while red circles and text are discordant. Ages reported are $^{207}\text{Pb}/^{206}\text{Pb} \pm 2\sigma$. Abbreviations: Bt—biotite, Ep—epidote, Mt—magnetite, Pl—plagioclase, Qtz—quartz, Scp—scapolite, Seri—sericite/white mica.

4.2. Lithochemistry

Lithochemistry results are shown in Figure 7a–e and full geochemistry results are presented in the Supplementary Table S2. On the Na- and K-metasomatism plot [88] (Figure 7a), all samples except two (008 and 017) indicate significant Na-alteration. The potassic-altered granite from Saarijärvi (sample 017) plots in the igneous spectrum, likely indicating a K-overprint of earlier Na-alteration, whereas the magnetite–ilmenite gabbro from Kalixforsbron (008) is interpreted as relatively unaltered. Accordingly, chemical classification plots were chosen to reduce the reliance on alkali concentrations and mobile elements. The R1–R2 chemical variation diagram [89] indicates that the felsic igneous intrusions are chemically granitic in character (granite to alkali granite) whereas the magnetite–ilmenite gabbro (008) plots in the theralite–gabbroic fields (Figure 7b). Sample 008 has anomalously low SiO₂ content (38.1 wt. %), possibly due to dilution by the high abundance of Fe-oxides. In the Yb vs. Ta discrimination plot [90] all the felsic plutonic samples fall within the volcanic-arc field (Figure 7c), though bordering with the syncollisional (005, 065, 017) and within-plate domains (017, 097). In the Ta/Hf vs. Th/Hf diagram [91], two samples (017, 065) plot on the border between within plate volcanic zone (WPVZ) and active continental margin fields (Figure 7d). The Archean sample (097) plots in the active continental margin field together with the sample 005. The spider diagram (Figure 7e) of REE concentrations normalized to C1 chondrite [92] indicates fractionation patterns with elevated light REE (LREE) and depleted heavy REE (HREE) and a strong negative Eu anomaly for the felsic intrusive samples 017 and 065 (Saarijärvi). However, sample 005 (Kalixforsbron) shows a strongly enriched LREE and strongly depleted HREE pattern with only a weak negative Eu anomaly. The magnetite–ilmenite gabbro (008, Kalixforsbron) shows a weak LREE enrichment (Figure 7e).

4.3. U-Pb Zircon Geochronology

The U-Pb data for all samples were assessed for concordia based on the relative discordia percent (percent difference between $^{238}\text{U}/^{206}\text{Pb} \pm 2\sigma$ of the data point and the concordia curve at a fixed $^{207}\text{Pb}/^{206}\text{Pb}$ value, i.e., assessed by the closest approach of the error ellipse on a 2σ level to concordia, Tables S3–S9) combined with the presence or absence of textural evidence (e.g., cracks, metamict domains, inclusions). Spots where discordant values correlated with textural evidence were removed from the calculations (Tables S3–S9). Weighted average $^{207}\text{Pb}/^{206}\text{Pb}$ ages were calculated after identification of a statistically coherent data population in concordia space. Weighted average ages are presented as the preferred crystallization age of the samples to account for possible sensitivity of the concordia ages to Pb/U inaccuracies. Uncertainties reported are 95% confidence a priori errors. For details of the U-Pb datasets, post-analysis spot descriptions, and details on data used or omitted in the age calculations, refer to Supplementary Tables S3–S9.

4.3.1. Kalixforsbron Area—Samples 005, 008

Thirty-four analyses were taken from zircon grains from sample 005 that yield U concentrations between 300 and 9440 ppm, Th/U ratios between 0.1 and 1.4, and common Pb (f_{206} %) values between 0.0 and 1.8% (Table S3). Neither a concordia nor weighted average age could be calculated for sample 005 due to most of the dataset yielding > 5% discordance. A lightly trimmed dataset removing the highly discordant points with correlating textural evidence (e.g., cracks) produces a weak discordia trend (MSWD = 5.2, $n = 26$) between ~1875 and ~470 Ma (Figure 8a). Although the results cannot be used to assign a statistically robust crystallization age for this sample, it can be concluded that this pluton intruded during the early orogenic phase of igneous activity in the Kiruna area.

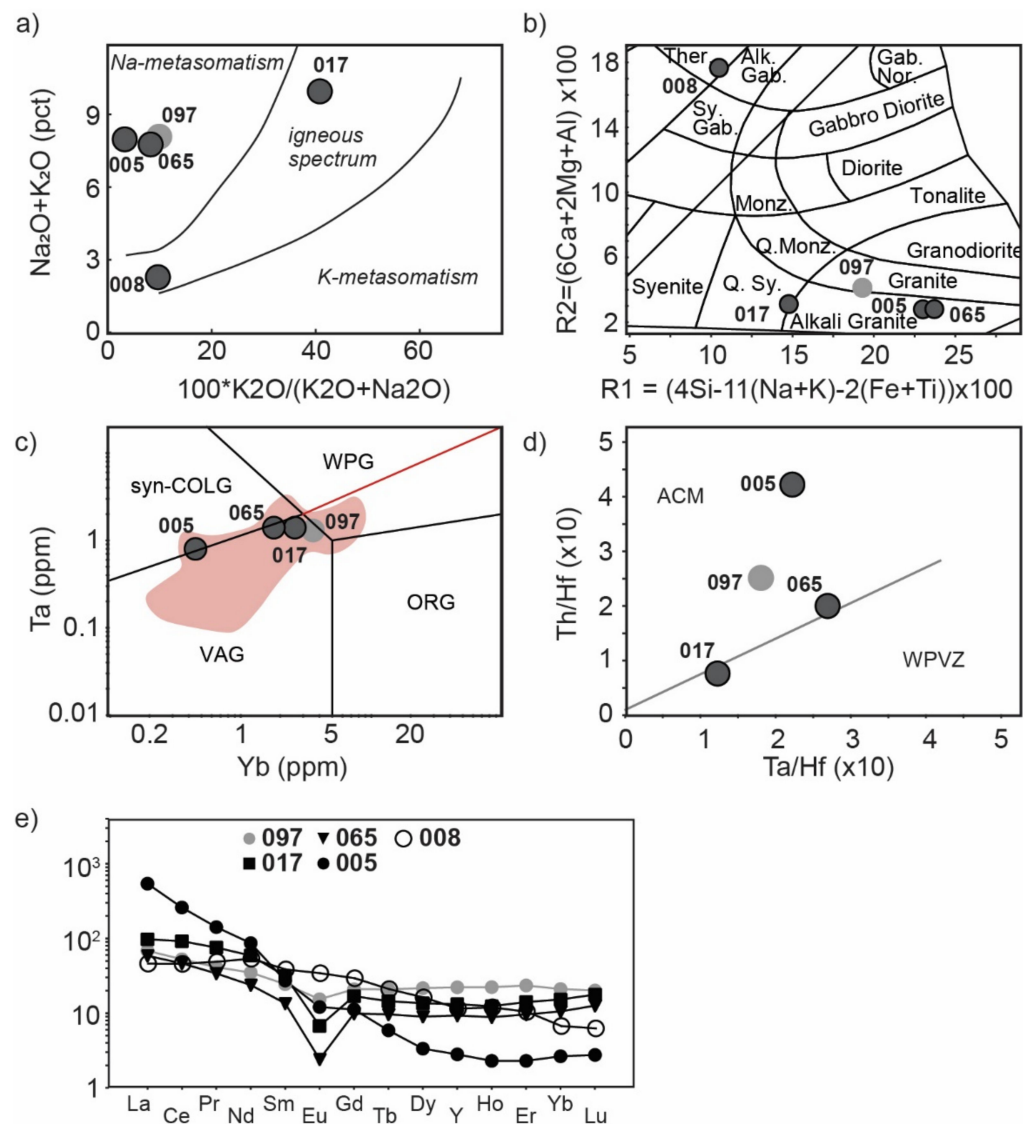


Figure 7. (a) Metasomatism diagram after Hughes [88]; (b) R1–R2 plutonic rock classification diagram [89]. Ther. = Theralite, Alk. Gab. = alkali gabbro, Gab. Nor. = gabbro norite, Sy. Gab. = syeno gabbro, Monz. = monzonite, Q. Monz. = quartz monzonite, Q. Sy. = quartz syenite. (c) Classification diagram for granitic rocks. Syn-COLG = syncollisional, WPG = within plate granite, VAG = volcanic arc granite, ORG = orogenic granite [90]. Pink field marks the Yb vs. Ta values of regional PMS samples [31]; (d) Ta/Hf vs. Th/Hf diagram delineating tectonic environments. ACM = active continental margin, WPVZ = within-plate volcanic zone [91]; (e) REE normalized to C1 Chondrite after Sun and McDonough [92].

Twelve analyses were taken from zircon grains from the magnetite–ilmenite gabbro (sample 008), which yield U concentrations between 20 and 840 ppm, Th/U ratios between 0.9 and 1.9, and common Pb (f_{206} %) values between 0.0 and 1.2% (Table S4). The data yield a mostly concordant U–Pb dataset (Figure 8b). Two discordant ellipses (defined by $\pm 1\%$ age discordance) correlating to spots overlapping with cracks were removed along with one concordant ellipse that had a high uncertainty (defined by the large ellipse size, Figure 8b). The remaining concordant data yield a weighted average $^{207}\text{Pb}/^{206}\text{Pb}$ age of 1877 ± 10 Ma (95%, MSWD = 1.3, $n = 9$; Figure 8b).

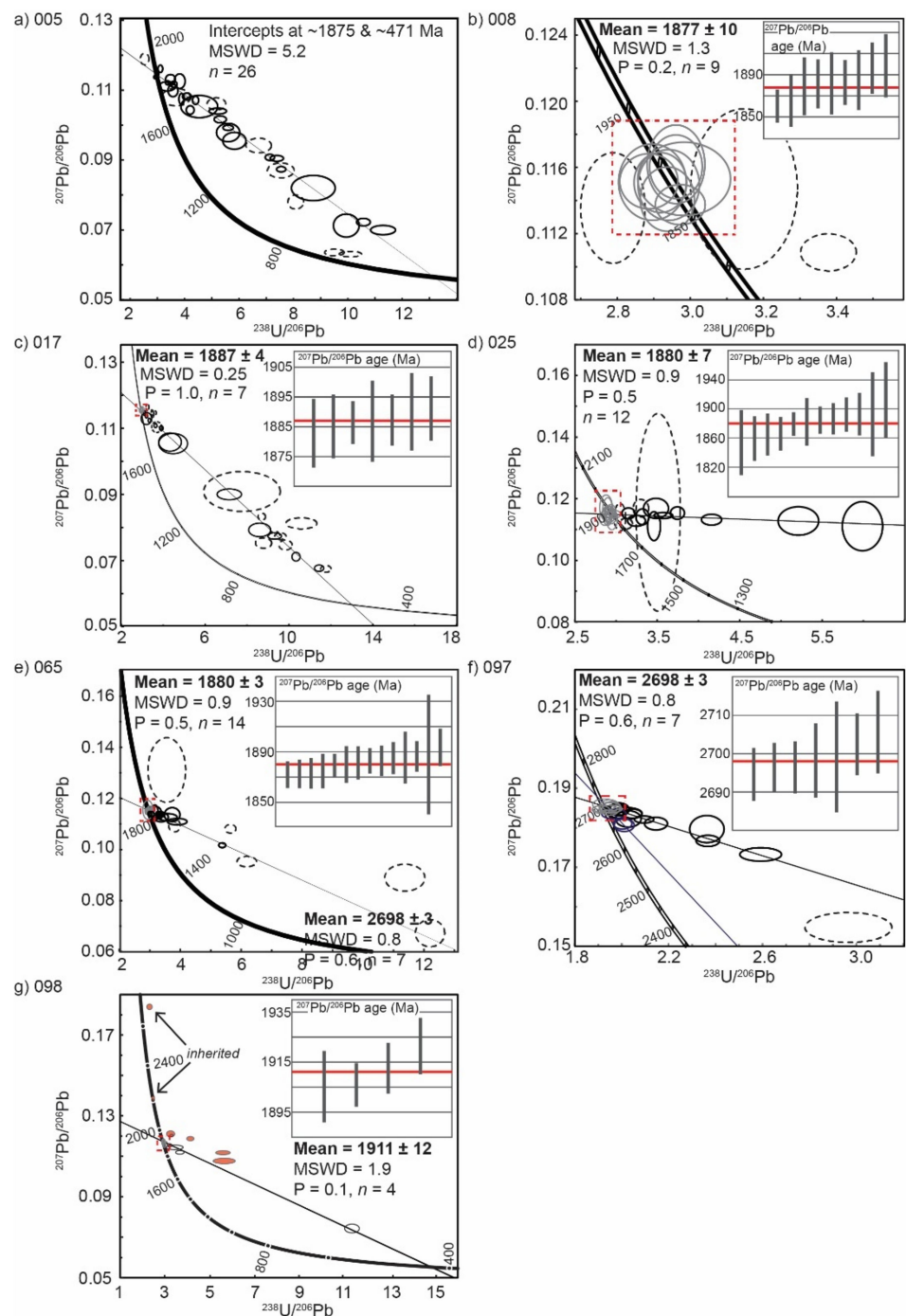


Figure 8. SIMS data in Tera–Wasserburg diagrams and $^{207}\text{Pb}/^{206}\text{Pb}$ weighted average plots for the samples: (a) 005; (b) 008; (c) 017; (d) 025; (e) 065; (f) 097; and (g) 098. Dashed black and red-filled circles represent data points left out of regression calculations. Gray circles represent data used for $^{207}\text{Pb}/^{206}\text{Pb}$ weighted average ages. Data point error ellipses and error bars are 2σ . The weighted average age is taken as the most reliable estimate of the crystallization age of the sample.

4.3.2. Saarijärvi Area—Samples 017, 025, 065, 097

Thirty-two analyses were taken from zircon grains from sample 017 that yield U concentrations between 250 and 7500 ppm, Th/U ratios between 0.4 and 2.0, and common Pb (f_{206} %) values between 0.0 and 1.2% (Table S5). The U–Pb dataset for sample 017 is relatively discordant, and a regression line through the spots with the least textural defects ($n = 20$) yields a weak discordia trend between ~ 1885 and ~ 477 Ma (Figure 8c). Eight ellipses (2σ) overlap the concordia curve; however, one analysis plots younger than the concordant

cluster with a $^{207}\text{Pb}/^{206}\text{Pb}$ age of 1848 ± 24 Ma (2σ) and is interpreted to possibly represent a late metamorphic zircon growth at the end of the early Svecokarelian crustal shortening phase (ca. 1.86 Ga). The remaining seven analyses yield a weighted average $^{207}\text{Pb}/^{206}\text{Pb}$ age of 1887 ± 4 Ma (95%, MSWD = 0.25, $n = 7$, Figure 8c), which is proposed to best represent the crystallization age of the sample.

Twenty-six analyses were taken from zircon grains from sample 025 which yield U concentrations between 20 and 510 ppm, Th/U ratios between 0.1 and 1.8, and common Pb (f_{206} %) values between 0.0 and 3.5% (Table S6). The U-Pb analyses for sample 025 show evidence of recent Pb loss with most of the discordant data deriving from analyses that intersected fractures. Three concordant analyses plot significantly away from the concordant cluster and were excluded from the age calculation. These spots each exhibited either textural evidence (e.g., interpreted mixed hydrothermal and igneous domains, cracks) or analytical uncertainty for exclusion. A regression line through the remaining dataset after trimming one additional discordant analysis intersecting a large crack yields an upper intercept age of ~ 1879 Ma ($n = 22$). Twelve concordant analyses from the sample yield a weighted average $^{207}\text{Pb}/^{206}\text{Pb}$ of 1880 ± 7 Ma (95%, MSWD = 0.9, $n = 12$, Figure 8d) and is interpreted as the most reliable crystallization age for the sample.

Thirty-eight analyses were taken from zircon grains from sample 065 that yield U concentrations between 160 and 4370 ppm, Th/U ratios between 0.3 and 1.2, and common Pb (f_{206} %) values between 0.0 and 1.6% (Table S7). The U-Pb data from sample 065 yield a weak discordia trend between ~ 1884 ($n = 32$) and ~ 447 Ma (Figure 8e) with minimal trimming of discordant data. Of the data overlapping the concordia curve, two analyses were removed from the age calculation because the 2σ error ellipse did not correlate statistically with the concordant cluster and have slightly younger $^{207}\text{Pb}/^{206}\text{Pb}$ ages. The resulting weighted average $^{207}\text{Pb}/^{206}\text{Pb}$ age is 1880 ± 3 Ma (95%, MSWD = 0.9, $n = 14$, Figure 8e) and is taken as the crystallization age of the sample.

Twenty-four analyses were taken from zircon grains from sample 097 that yield U concentrations between 120 and 740 ppm, Th/U ratios between 0.3 and 1.1, and common Pb (f_{206} %) values between 0.0 and 0.6% (Table S8). The U-Pb data for sample 097 yield an Archean age from both the regression line and the concordia cluster. Two different regression lines (Figure 8f) can be observed reflecting a disturbance in the U-Pb isotopic system at ca. 1.78 and 0.7 Ga. Both regression lines show an upper intercept age of about 2700 Ma. A concordant cluster ($n = 7$) yields a weighted average $^{207}\text{Pb}/^{206}\text{Pb}$ age of 2698 ± 3 Ma (95%, MSWD = 0.8, $n = 7$, Figure 8f), which is taken as the best estimate for the age of crystallization.

4.3.3. Pahtohavare Area—Sample 098

Sixteen analyses were taken from zircon grains from sample 098 which yield U concentrations between 190 and 2060 ppm, Th/U ratios between 0.1 and 1.3, and common Pb (f_{206} %) values between 0.0 and 2.6% (Table S9). The U-Pb data from sample 098 indicate that two zircon grains are inherited with apparently different $^{207}\text{Pb}/^{206}\text{Pb}$ ages (one discordant at 2688.8 ± 4.9 and one concordant at 2210.2 ± 7.2 Ma, Figure 8g). A regression line through the data, excluding the inherited points and other spots with textural defects, results in a weak discordia trend between ~ 1910 and ~ 418 Ma (Figure 8g). Only a few data points ($n = 4$) are concordant, which yield a weighted average $^{207}\text{Pb}/^{206}\text{Pb}$ age of 1911 ± 12 Ma (95% confidence, MSWD = 1.9, $n = 4$, Figure 8g). The weighted average $^{207}\text{Pb}/^{206}\text{Pb}$ age is interpreted to best represent the age of the sample.

5. Discussion

Assessing the energy drive of the mineral systems in the Kiruna mining district is one of the critical aspects for a holistic understanding of IOA and IOCG genesis and relationships. While the timing of the IOA deposits regionally shows a strong temporal affinity to the early Svecokarelian orogeny [5,23–25,27,28,63], increasing geochronological evidence indicates that Cu mineralization occurs both early and late (cf. [5,27]), drawing into question

the relative timing of the largely undated Cu-mineralization in the Kiruna mining district. Regionally, at least two distinct periods of magmatotectonism occurred during the Svecokarelian orogeny [2], and in the Kiruna district, the question remains unresolved for what role these time-separated events played on the IOA and IOCG mineral systems. The following sections discuss the geochronology and lithogeochemical data and implications these results have on understanding the energy drive for the mineralization in Kiruna.

5.1. Early Igneous Activity

The oldest sample collected in the study is an Archean granite (sample 097) in the Saarijärvi area, and the age obtained (2698 ± 3 Ma, Figure 8f) confirms a previous Archean age determination for this intrusive body (2710 ± 4 ; [87]). It is the only known exposure of Archean rock in the Kiruna mining district. The sample shows strong Na-alteration in the lithogeochemistry data (Figure 7a) whereas evidence for potassic alteration is lacking.

Sample 098 from the southwestern side of the NW–SE trending shear zone in Pahtohavare was taken from an area mapped as the Porphyrite group [64]. The large plagioclase phenocrysts and amygdales found in the sample (Figure 6) agree with previous descriptions of Porphyrite group volcanics [40,93]. The sample yields a weighted average $^{207}\text{Pb}/^{206}\text{Pb}$ age of 1911 ± 12 Ma (Figure 8g), which is older than the typical age for the group (ca. 1.89–1.88 Ga, [56]) but consistent with being slightly older than the Kiirunavaara group (e.g., Hopukka and Luossavaara formations, ca. 1.88–1.86 Ga [28,93], Figure 3). This age, together with a recent age determination by Andersson et al. [22] on a volcanic intercalation in the Kurravaara conglomerate (1887 ± 3 Ma), mark the earliest Orosirian volcanic activity determined in the Kiruna district.

5.2. Timing of the Magnetite–Ilmenite Gabbro Intrusion and Possible Relation to IOA Deposits

The age obtained from the magnetite–ilmenite gabbro (1877 ± 10 Ma, sample 008, Figure 8b) is the first age determination of a mafic pluton in Kiruna. The gabbro is enriched in iron oxides with approximately 15%–20% magnetite–ilmenite modal abundance, and ca. 23% $\text{Fe}_2\text{O}_3(\text{total})$ content. Apatite also occurs abundantly in the sample and was noted as the primary nonmagnetic heavy mineral in the final concentrates of mineral extraction for age dating. It is also SiO_2 -poor (38.1 wt. %) and falls below the typical gabbroic silica content in classification diagrams (45%–52%, [94]), which may be explained by dilution due to the high amount of magnetite and ilmenite. The zircon grains from the sample are rounded with bright rims in CL imagery (Figure 4g), and consequently the possibility that these zircon grains are inherited based on the rounded shape and bright rims cannot be excluded. Therefore, the 1877 ± 10 Ma age obtained is conservatively interpreted as the maximum age of the gabbro rather than the absolute age of crystallization. However, the deformation zone that cross-cuts the gabbro, which is characterized by brecciated and potassic-altered gabbroic clasts with quartz infill, suggests that the pluton was emplaced prior to brittle–ductile D_2 deformation, tentatively placing it into the early Svecokarelian timeframe.

Although no direct genetic link can be made, the approximate timing of formation for this intrusion (1877 ± 10 Ma) overlaps with the zircon U–Pb SIMS age of the IOA emplacement in Kiruna (1877 ± 4 Ma, 1874 ± 7 Ma), determined from zircon grains extracted from magnetite ore samples [28]. The zircon grains dated by Westhues et al. [28] show complex textural characteristics including thin oscillatory zoning in the cores, irregular patchy textures, and rims with very bright CL responses. The zircon grains from the gabbro in this study do not show irregular patchy textures but share the characteristic of thin oscillatory zoning and very bright rims in CL. Troll et al. [95] obtained $\delta^{56}\text{Fe}$ and $\delta^{18}\text{O}$ isotopic data from the Kiirunavaara IOA deposit that overlap with high temperature igneous and volcanic reference materials, supporting the influence of magmatic processes for the iron oxide–apatite ore. The age-dated magnetite ores from Kiruna show a juvenile signature in both $\epsilon\text{Hf}_i\text{-}(\text{zircon})$ and $\epsilon\text{Nd}_i\text{-}(\text{whole rock})$ data, which were interpreted to indicate that the ore components derived from the mafic volcanic rocks of the Kiruna greenstone group [58,72]. Leaching of the greenstones in the Kiruna mining district as a mechanism to

provide iron during the IOA ore formation was argued for by Parák [96], but the model is not appropriate for other IOA deposits in Norrbotten, such as in the Gällivare district where no greenstone stratigraphy has been recorded. However, the Gällivare district also hosts a large magnetite-bearing [97] ultramafic–mafic layered complex (Dundret) that was dated to be 1883 ± 5 Ma [33], overlapping with the back-arc extension phase of the Svecokarelian orogeny and timing of IOA emplacement. The results of the current study show that both the Kiruna and Gällivare mining districts (host to the giant Kiirunavaara and Malmberget IOA deposits, respectively) have contemporaneous relationships with mafic Fe-bearing magmatism. The intrusion of mafic magma into a crustal setting hosting evaporitic sequences and a consequential unmixing of iron-rich and volatile-rich melts has been suggested as a model for IOA deposits in Norrbotten [5] and elsewhere [15,98,99]. In the Kiruna mining district, the U-Pb geochronology data from this study suggest that the generation of mafic Fe-rich magmatism seen in the Kalixforsbron area can be an alternative candidate for contributing to the juvenile $\epsilon\text{Hf}_i\text{-}(\text{zircon})$ and $\epsilon\text{Nd}_i\text{-}(\text{whole rock})$ signatures presented by Westhues et al. [58,72], which is supported by U-Pb geochronology data.

5.3. Energy Drive Insights for the Mineral System

Overall, the zircon U-Pb age results show that abundant thermal activity was occurring in the Kiruna mining district during the early stage of the Svecokarelian orogeny from ca. 1923–1867 Ma (including age uncertainties, Figure 8). The Ta/Hf and Th/Hf ratios of the samples reflect an active continental margin bordering to within-plate environments for the felsic early orogenic magmatism (Figure 7d). Furthermore, Yb vs. Ta values show the intrusions fall within the volcanic arc field and border the within-plate granite fields (Figure 7c). Though relatively few data points exist in this study, the bordering tendency of tectonic environment agrees with the observed trend for the Kiirunavaara group intermediate–felsic volcanics in the Gällivare district [33] and for PMS intrusive rocks regionally (cf. [31], Figure 7c). The volcanic arc signatures, the mafic to felsic compositional range of the intrusions, the distance to the coeval subduction zone [100], the occurrence of thick basaltic layers in the Kiirunavaara group west of Kiruna [2], and the basin stratigraphy of the Kiruna mining district [21], support an extensional back-arc environment for the northern Norrbotten region at the onset of the Svecokarelian orogeny.

Sodic alteration is recorded in all of the felsic plutonic samples (Figure 7a) reflecting the early regional Na-Ca metasomatism and additionally bracketing the maximum age of the metasomatism to syn- to post-magmatic activity. The alteration likely resulted from the elevated heat and fluid flow caused by magmatism, and the hydrothermal fluids subsequently mobilized components from highly saline sources and channeled them into large-scale shear zones [35] facilitating the widespread distribution. Only sample 017 (from Saarijärvi) shows evidence for a K-overprint indicated by coarse patchy quartz–K-feldspar alteration and elevated K_2O content. K-alteration manifests as local hydrothermal alteration proximal to ore deposits within the Kiruna mining district (e.g., hanging wall to the Per Geijer IOA ores, Rakkurijärvi IOCG; [5,26,28,101]); however, it is also observed affecting other rocks in the district (e.g., Kurraavaara conglomerate, along brittle fracture planes, in brittle fault structures) indicating that a regional potassic alteration also affected the district.

The model age of sample 025 (1880 ± 7 Ma) from an outcrop in the Saarijärvi area contradicts the much younger age (1792 ± 4 Ma; U-Pb ICP–MS titanite and zircon) of the same locality (from drill core) presented by Romer et al. [24] and agrees with the other early Svecokarelian ages from the Saarijärvi area obtained in this study. Our results indicate that the crystallization of these igneous bodies occurred at the transition from extension to early D_1 compression stage [2,20,21,102] of the tectonic evolution and question the extent of late orogenic magmatism in the Kiruna area. However, it is clear that the Svecokarelian orogeny affected the zircon grains as recorded by zonation, dissolutions, and regrowth textures (Figure 5f), which occasionally yield $^{207}\text{Pb}/^{206}\text{Pb}$ individual spot ages around 1.80 Ga (Supplementary Tables S3–S7), in agreement with tectonothermal activity in a nearby shear zone [22].

The geochronology results of this study unanimously point to abundant early Svecokarelian intrusive activity and thermal drive in the Kiruna mining district. Despite this, a late thermal drive and magmatic influence cannot be excluded when other factors are considered. First, though K-alteration exhibits large variation regionally, a characteristic potassic–ferroan (e.g., K-feldspar, quartz, biotite, magnetite, epidote) alteration occurs in relation to granitoids and pegmatites of the late orogenic Lina suite [18,20]. In the Kiruna mining district, K-feldspar coatings are often observed in late structural features. Additionally, patchy quartz–K-feldspar alteration is observed affecting rocks without any known proximity to mineralization such as at sample locality 017 (Figure 5a). At various localities in the Kurravaara conglomerate (e.g., at the contact with the Kiruna greenstone group in the Pahtohavare area and to the west of Luossavaara; Figure 2), a feldspar–epidote–magnetite hydrothermal alteration assemblage occurs in late structural features, in patchy textures, and around clast rims. These observations suggest a late orogenic K-alteration affected the district, possibly linked to late magmatic fluid circulation. Second, the late orogenic magmatic rocks are regionally voluminous and outcrop extensively just outside of the Kiruna area (Figure 1). Tavakoli et al. [103] recently showed potential field modeling results that indicate these intrusions have sheetlike geometries and it may be possible that similar sheetlike intrusions underly parts of the Kiruna area that are inaccessible to sampling. Faults and shear zones in the Kiruna mining district likely played an important role for the transport of fluids and heat, and recent work has shown that basin inversion during D₂ affected the district with many fault zones being reactivated, including the northern continuation of the shear zone hosting the Rakkurijärvi IOCG deposit [21]. Andersson et al. [21] further noted that Cu-Fe sulfides occur in brittle structures kinematically constrained to this late orogenic phase. This observation, when placed in a tectonic context and viewed from a mineral systems perspective, argues that some late mineralization or remobilization occurred in the Kiruna mining district, even though the geochronology data from this study indicate a single thermal driving event tied to the early phase. It is possible that the results do not apply completely to all other parts of the district, as deeper and unexposed intrusions may exist. However, more geochronological and mineral systems studies should be done to further understand the nature and timing of the IOA and IOCG systems.

6. Conclusions

This study used a mineral systems approach constrained by a regional tectonic framework to investigate the timing of energy drives related to the Kiruna mining district mineral systems. The U-Pb zircon geochronology conducted provides valuable new age data for intrusions in the Kiruna mining district and insight into the thermal drive for the mineral systems. The dated intrusions were sampled from the southern part of the district where Cu ± Au and IOCG mineralization occur in spatial proximity to plutonic bodies. New ages were obtained on the Archean basement (2698 ± 3 Ma) and a volcanic rock (1911 ± 12 Ma) interpreted to belong to the Porphyry group. Results from mafic to felsic plutonic rocks yield ages that overlap with the early Svecokarelian magmatic period (ca. 1923–1867 Ma including age uncertainties) and illustrate that abundant magmatic activity was occurring in the Kiruna mining district during that time, which likely provided heat (and possibly metals and fluids) to drive the early IOA- and IOCG-related mineral systems. A weighted average $^{207}\text{Pb}/^{206}\text{Pb}$ age of 1887 ± 10 Ma for a magnetite–ilmenite gabbroic pluton overlaps in age with the Kiirunavaara IOA deposit and marks the second district (along with the Gällivare district) that has giant IOA deposits forming coevally with large Fe-oxide-rich mafic magmatism. No late Svecokarelian ages were obtained in this study, despite sampling a syenitic pluton previously dated to have crystallized in the late phase of the Svecokarelian orogeny (D₂). Our sample yielded a weighted average $^{207}\text{Pb}/^{206}\text{Pb}$ age of 1880 ± 7 Ma. However, the extensive and voluminous nature of the late magmatism regionally and observation of potassic alteration in the district suggest that a deeper or more distal thermal influence of late orogenic magmatism still played a role in the late mineral system.

Supplementary Materials: The following supporting information can be downloaded at: <https://www.mdpi.com/article/10.3390/min12070875/s1>, Table S1: U-Pb ion-microprobe/SIMS data for secondary standard M257 over the analytical sessions; Table S2: Bulk rock major and trace element litho-geochemistry results of samples from the southern Kiruna Mining District; Table S3: Zircon U-Pb ion-microprobe/SIMS data for sample 005. Spot numbers are in row (r) grain (g) format with a and b delineating multiple spots in the same grain. M. zone = middle zone; Table S4: Zircon U-Pb ion-microprobe/SIMS data for sample 008. Spot numbers are in row (r) grain (g) format with a and b delineating multiple spots in the same grain. M. zone = middle zone; Table S5: Zircon U-Pb ion-microprobe/SIMS data for sample 017. Spot numbers are in column (c) grain (g) format with a and b delineating multiple spots in the same grain; Table S6: Zircon U-Pb ion-microprobe/SIMS data for sample 025. Spot numbers are in row (r) grain (g) format with a and b delineating multiple spots in the same grain; Table S7: Zircon U-Pb ion-microprobe/SIMS data for sample 065. Spot numbers are in row (r) grain (g) format with a and b delineating multiple spots in the same grain. M. zone = middle zone; Table S8: Zircon U-Pb ion-microprobe/SIMS data for sample 097. Spot numbers are in row (r) grain (g) format with a, b, and c delineating multiple spots in the same grain. M. zone = middle zone; Table S9: Zircon U-Pb ion-microprobe/SIMS data for sample 098. Spot numbers are in row (r) grain (g) format with a and b delineating multiple spots in the same grain. M. zone = middle zone.

Author Contributions: Conceptualization, L.L. and T.E.B.; methodology, L.L., J.B.H.A., T.E.B. and M.J.W.; data curation, M.J.W.; validation, M.J.W.; formal analysis, L.L.; visualization, L.L.; funding acquisition, T.E.B.; supervision, T.E.B. and O.M.; writing—original draft, L.L.; writing—review and editing, L.L., J.B.H.A., M.J.W., O.M. and T.E.B. All authors have read and agreed to the published version of the manuscript.

Funding: This work is funded by the European Union’s Horizon 2020 project “New Exploration Technologies—NEXT” (Grant Agreement No. 776804). NordSIMS was supported by a Swedish Research Council infrastructure grant (2017-00671) at the time of analysis.

Data Availability Statement: Data are available within the article or in Supplementary Materials.

Acknowledgments: The staff at the Geological Survey of Sweden is thanked for their collaboration and help during the sampling campaigns at the National Drill Core Archive in Malå. Staff at the NordSIMS laboratory at the Swedish Museum of Natural History in Stockholm are thanked for the sample preparation and for performing the SIMS analyses of zircon; this is NordSIMS contribution #714. We further thank Thomas Aiglsperger at the QanTmin laboratories, LTU, for training and access to the zircon extraction equipment, and Nils Jansson (LTU) for providing helpful guidance with the litho-geochemistry. The authors thank three reviewers for their constructive comments on this study.

Conflicts of Interest: The authors declare no conflict of interest.

References

1. Hitzman, M.W.; Oreskes, N.; Einaudi, M.T. Geological characteristics and tectonic setting of Proterozoic iron oxide (Cu-U-Au-REE) deposits. *Precambrian Res.* **1992**, *58*, 241–287. [[CrossRef](#)]
2. Bergman, S.; Kübler, L.; Martinsson, O. *Description of Regional Geological and Geophysical Maps of Northern Norrbotten County (East of the Caledonian Orogen)*; Ba56; Sveriges geologiska undersökning: Uppsala, Sweden, 2001; ISBN 978-91-7158-643-8.
3. Williams, P.J.; Barton, M.D.; Johnson, D.A.; Fontboté, L.; De Haller, A.; Mark, G.; Oliver, N.H.S.; Marschik, R. Iron Oxide Copper-Gold Deposits—Geology, Space-Time Distribution, and Possible Modes of Origin. In *Economic Geology: One Hundredth Anniversary Volume*; Society of Economic Geologists: Littleton, CO, USA, 2005; pp. 371–405. ISBN 978-1-887483-01-8.
4. Barton, M.D. Iron Oxide (–Cu–Au–REE–P–Ag–U–Co) Systems. In *Treatise on Geochemistry*; Elsevier: Amsterdam, The Netherlands, 2014; pp. 515–541. ISBN 978-0-08-098300-4.
5. Martinsson, O.; Billström, K.; Broman, C.; Weihed, P.; Wanhainen, C. Metallogeny of the Northern Norrbotten Ore Province, northern Fennoscandian Shield with emphasis on IOCG and apatite-iron ore deposits. *Ore Geol. Rev.* **2016**, *78*, 447–492. [[CrossRef](#)]
6. Groves, D.I.; Bierlein, F.P.; Meinert, L.D.; Hitzman, M.W. Iron Oxide Copper-Gold (IOCG) Deposits through Earth History: Implications for Origin, Lithospheric Setting, and Distinction from Other Epigenetic Iron Oxide Deposits. *Econ. Geol.* **2010**, *105*, 641–654. [[CrossRef](#)]
7. Skirrow, R.G. Iron oxide copper-gold (IOCG) deposits—A review (part 1): Settings, mineralogy, ore geochemistry, and classification. *Ore Geol. Rev.* **2021**, *140*, 104569. [[CrossRef](#)]
8. Sillitoe, R.H. Iron oxide-copper-gold deposits: An Andean view. *Miner. Depos.* **2003**, *38*, 787–812. [[CrossRef](#)]
9. Corriveau, L.; Montreuil, J.-F.; Potter, E.G. Alteration Facies Linkages Among Iron Oxide Copper-Gold, Iron Oxide-Apatite, and Affiliated Deposits in the Great Bear Magmatic Zone, Northwest Territories, Canada. *Econ. Geol.* **2016**, *111*, 2045–2072. [[CrossRef](#)]

10. Barra, F.; Reich, M.; Selby, D.; Rojas, P.; Simon, A.; Salazar, E.; Palma, G. Unraveling the origin of the Andean IOCG clan: A Re-Os isotope approach. *Ore Geol. Rev.* **2017**, *81*, 62–78. [[CrossRef](#)]
11. Simon, A.C.; Knipping, J.; Reich, M.; Barra, F.; Deditius, A.P.; Bilenker, L.; Childress, T. Kiruna-Type Iron Oxide-Apatite (IOA) and Iron Oxide Copper-Gold (IOCG) Deposits Form by a Combination of Igneous and Magmatic-Hydrothermal Processes: Evidence from the Chilean Iron Belt. In *Metals, Minerals, and Society*; Society of Economic Geologists (SEG): Littleton, CO, USA, 2018; ISBN 978-1-62949-308-4.
12. Tornos, F. Magnetite-Apatite and IOCG deposits formed by magmatic-hydrothermal evolution of complex calc-alkaline melts. In Proceedings of the Eleventh Biennial SGA Meeting, Antofagasta, Chile, 26–29 September 2011; pp. 26–28.
13. Nyström, J.O.; Henriquez, F. Magmatic features of iron ores of the Kiruna type in Chile and Sweden; ore textures and magnetite geochemistry. *Econ. Geol.* **1994**, *89*, 820–839. [[CrossRef](#)]
14. Naslund, H.R.; Henríquez, F.; Nyström, J.O.; Vivallo, W.; Dobbs, F.M. Magmatic iron ores and associated mineralisation: Examples from the Chilean High Andes and Coastal Cordillera. In *Hydrothermal Iron Oxide-Copper-Gold & Related Deposits: A Global Perspective*; PCG Publishing: Adelaide, Australia, 2002; Volume 2, pp. 207–226.
15. Velasco, F.; Tornos, F.; Hanchar, J.M. Immiscible iron- and silica-rich melts and magnetite geochemistry at the El Laco volcano (northern Chile): Evidence for a magmatic origin for the magnetite deposits. *Ore Geol. Rev.* **2016**, *79*, 346–366. [[CrossRef](#)]
16. Tornos, F.; Velasco, F.; Hanchar, J.M. The Magmatic to Magmatic-Hydrothermal Evolution of the El Laco Deposit (Chile) and Its Implications for the Genesis of Magnetite-Apatite Deposits. *Econ. Geol.* **2017**, *112*, 1595–1628. [[CrossRef](#)]
17. Wyborn, L.A.I.; Heinrich, C.A.; Jaques, A.L. Australian Proterozoic Mineral Systems: Essential Ingredients and Mappable Criteria. In Proceedings of the Australasian Institute of Mining and Metallurgy Publication Series, Darwin, Australia, 5 August 1994; Volume 94, pp. 109–115.
18. Bauer, T.E.; Andersson, J.B.H.; Sarlus, Z.; Lund, C.; Kearney, T. Structural Controls on the Setting, Shape, and Hydrothermal Alteration of the Malmberget Iron Oxide-Apatite Deposit, Northern Sweden. *Econ. Geol.* **2018**, *113*, 377–395. [[CrossRef](#)]
19. Bauer, T.E.; Lynch, E.P.; Sarlus, Z.; Drejning-Carroll, D.; Martinsson, O.; Metzger, N.; Wanhainen, C. Structural Controls on Iron Oxide Copper-Gold Mineralization and Related Alteration in a Paleoproterozoic Supracrustal Belt: Insights from the Nautanen Deformation Zone and Surroundings, Northern Sweden. *Econ. Geol.* **2022**, *117*, 327–359. [[CrossRef](#)]
20. Andersson, J.B.H.; Bauer, T.E.; Lynch, E.P. Evolution of structures and hydrothermal alteration in a Palaeoproterozoic supracrustal belt: Constraining paired deformation–fluid flow events in an Fe and Cu–Au prospective terrain in northern Sweden. *Solid Earth* **2020**, *11*, 547–578. [[CrossRef](#)]
21. Andersson, J.B.H.; Bauer, T.E.; Martinsson, O. Structural Evolution of the Central Kiruna Area, Northern Norrbotten, Sweden: Implications on the Geologic Setting Generating Iron Oxide-Apatite and Epigenetic Iron and Copper Sulfides. *Econ. Geol.* **2021**, *116*, 1981–2009. [[CrossRef](#)]
22. Andersson, J.B.H.; Logan, L.; Martinsson, O.; Chew, D.; Kooijman, E.; Kielman-Schmitt, M.; Kampmann, T.C.; Bauer, T.E. U–Pb zircon-titanite-apatite age constraints on basin development and basin inversion in the Kiruna mining district, Sweden. *Precambrian Res.* **2022**, *372*, 106613. [[CrossRef](#)]
23. Cliff, R.A.; Rickard, D.; Blake, K. Isotope systematics of the Kiruna magnetite ores, Sweden; Part 1, Age of the ore. *Econ. Geol.* **1990**, *85*, 1770–1776. [[CrossRef](#)]
24. Romer, R.L.; Martinsson, O.; Perdahl, J.A. Geochronology of the Kiruna iron ores and hydrothermal alterations. *Econ. Geol.* **1994**, *89*, 1249–1261. [[CrossRef](#)]
25. Storey, C.D.; Smith, M.P.; Jeffries, T.E. In Situ LA-ICP-MS U–Pb dating of metavolcanics of Norrbotten, Sweden: Records of extended geological histories in complex titanite grains. *Chem. Geol.* **2007**, *240*, 163–181. [[CrossRef](#)]
26. Smith, M.; Coppard, J.; Herrington, R.; Stein, H. The Geology of the Rakkurijärvi Cu-(Au) Prospect, Norrbotten: A New Iron Oxide-Copper-Gold Deposit in Northern Sweden. *Econ. Geol.* **2007**, *102*, 393–414. [[CrossRef](#)]
27. Smith, M.P.; Storey, C.D.; Jeffries, T.E.; Ryan, C. In Situ U–Pb and Trace Element Analysis of Accessory Minerals in the Kiruna District, Norrbotten, Sweden: New Constraints on the Timing and Origin of Mineralization. *J. Petrol.* **2009**, *50*, 2063–2094. [[CrossRef](#)]
28. Westhues, A.; Hanchar, J.M.; Whitehouse, M.J.; Martinsson, O. New Constraints on the Timing of Host-Rock Emplacement, Hydrothermal Alteration, and Iron Oxide-Apatite Mineralization in the Kiruna District, Norrbotten, Sweden. *Econ. Geol.* **2016**, *111*, 1595–1618. [[CrossRef](#)]
29. Wanhainen, C.; Billström, K.; Martinsson, O.; Stein, H.; Nordin, R. 160 Ma of Magmatic/Hydrothermal and Metamorphic Activity in the Gällivare Area: Re–Os Dating of Molybdenite and U–Pb Dating of Titanite from the Aitik Cu–Au–Ag Deposit, Northern Sweden. *Miner. Depos.* **2005**, *40*, 435–447. [[CrossRef](#)]
30. Knox-Robinson, C.M.; Wyborn, L.A.I. Towards a holistic exploration strategy: Using Geographic Information Systems as a tool to enhance exploration. *Aust. J. Earth Sci.* **1997**, *44*, 453–463. [[CrossRef](#)]
31. Bergman, S.; Weihed, P. Chapter 3 Archean (>2.6 Ga) and Paleoproterozoic (2.5–1.8 Ga), pre- and syn-orogenic magmatism, sedimentation and mineralization in the Norrbotten and Överkalix lithotectonic units, Svecokarelian orogen. *Geol. Soc. Lond. Mem.* **2020**, *50*, 27–81. [[CrossRef](#)]
32. Bergman, S.; Billström, K.; Persson, P.-O.; Skiöld, T.; Evins, P. U–Pb age evidence for repeated Palaeoproterozoic metamorphism and deformation near the Pajala shear zone in the northern Fennoscandian shield. *GFF* **2006**, *128*, 7–20. [[CrossRef](#)]

33. Sarlus, Z.; Andersson, U.B.; Martinsson, O.; Bauer, T.E.; Wanhainen, C.; Andersson, J.B.H.; Whitehouse, M.J. Timing and origin of the host rocks to the Malmberget iron oxide-apatite deposit, Sweden. *Precambrian Res.* **2020**, *342*, 105652. [[CrossRef](#)]
34. Lindblom, S.; Broman, C.; Martinsson, O. Magmatic-hydrothermal fluids in the Pahtohavare Cu-Au deposit in greenstone at Kiruna, Sweden. *Miner. Depos.* **1996**, *31*, 307–318. [[CrossRef](#)]
35. Frietsch, R.; Tuisku, P.; Martinsson, O.; Perdahl, J.-A. Early Proterozoic Cu-(Au) and Fe ore deposits associated with regional Na-Cl metasomatism in northern Fennoscandia. *Ore Geol. Rev.* **1997**, *12*, 1–34. [[CrossRef](#)]
36. Gleeson, S.A.; Smith, M.P. The sources and evolution of mineralising fluids in iron oxide–copper–gold systems, Norrbotten, Sweden: Constraints from Br/Cl ratios and stable Cl isotopes of fluid inclusion leachates. *Geochim. Cosmochim. Acta* **2009**, *73*, 5658–5672. [[CrossRef](#)]
37. Smith, M.P.; Gleeson, S.A.; Yardley, B.W.D. Hydrothermal fluid evolution and metal transport in the Kiruna District, Sweden: Contrasting metal behaviour in aqueous and aqueous–carbonic brines. *Geochim. Cosmochim. Acta* **2013**, *102*, 89–112. [[CrossRef](#)]
38. Bernal, N.F.; Gleeson, S.A.; Smith, M.P.; Barnes, J.D.; Pan, Y. Evidence of multiple halogen sources in scapolites from iron oxide-copper-gold (IOCG) deposits and regional Na Cl metasomatic alteration, Norrbotten County, Sweden. *Chem. Geol.* **2017**, *451*, 90–103. [[CrossRef](#)]
39. Storey, C.D.; Smith, M.P. Metal source and tectonic setting of iron oxide-copper-gold (IOCG) deposits: Evidence from an in situ Nd isotope study of titanite from Norrbotten, Sweden. *Ore Geol. Rev.* **2017**, *81*, 1287–1302. [[CrossRef](#)]
40. Martinsson, O. Geology and Metallogeny of the Northern Norrbotten Fe-Cu-Au Province. In *Soeconfennian Ore-Forming Environments of Northern Sweden-Volcanic Associated Zn-Cu-Au-Ag, Intrusion Related Cu-Au, Sediment Hosted Pb-Zn, and Magnetite-Apatite Deposits in Northern SWEDEN*; Guide Book Series; Allen, R.L., Martinsson, O., Weihed, P., Eds.; Society of Economic Geologists: Littleton, CO, USA, 2004; pp. 131–148.
41. Martinsson, O. Bedrock map 30J Rensjön NO, Sver. Geol. Undersökning Map, Serie Ai 132, Uppsala, Sweden. 1999. Available online: <https://resource.sgu.se/dokument/publikation/ai/ai132karta/ai132-karta.pdf> (accessed on 17 May 2022).
42. Pharaoh, T.C.; Pearce, J.A. Geochemical evidence for the geotectonic setting of early Proterozoic metavolcanic sequences in Lapland. *Precambrian Res.* **1984**, *25*, 283–308. [[CrossRef](#)]
43. Martinsson, O. Tectonic Setting and Metallogeny of the Kiruna Greenstones. Ph.D. Thesis, Luleå Tekniska Universitet, Lulea, Sweden, 1997.
44. Lahtinen, R.; Garde, A.A.; Melezhik, V.A. Paleoproterozoic evolution of Fennoscandia and Greenland. *Episodes* **2008**, *31*, 20–28. [[CrossRef](#)] [[PubMed](#)]
45. Bingen, B.; Solli, A.; Viola, G.; Torgersen, E.; Sandstad, J.S.; Whitehouse, M.J.; Røhr, T.S.; Ganerød, M.; Nasuti, A. Geochronology of the Palaeoproterozoic Kautokeino Greenstone Belt, Finnmark, Norway: Tectonic implications in a Fennoscandia context. *Nor. J. Geol.* **2015**, *95*, 365–396. [[CrossRef](#)]
46. Öhlander, B.; Skiöld, T.; Elming, S.-Å.; Claesson, S.; Nisca, D.H. Delineation and character of the Archaean-Proterozoic boundary in northern Sweden. *Precambrian Res.* **1993**, *64*, 67–84. [[CrossRef](#)]
47. Weihed, P.; Williams, P.J. Metallogeny of the northern Fennoscandian Shield: A set of papers on Cu–Au and VMS deposits of northern Sweden. *Min. Depos.* **2005**, *40*, 347–350. [[CrossRef](#)]
48. Bauer, T.E.; Andersson, J.B.H. Structural controls on Cu-Au mineralization in the Svappavaara area, northern Sweden: The northern continuation of the Nautanen IOCG-system (paper II). In *Paleoproterozoic Deformation in the Kiruna-Gällivare Area in Northern Norrbotten, Sweden: Setting, Character, Age, and Control of Iron Oxide-Apatite Deposits (Ph.D. Thesis)*; Andersson, J.B.H., Ed.; Luleå University of Technology: Luleå, Sweden, 2021; pp. 1–15.
49. Grigull, S.; Berggren, R.; Jönberger, J.; Jönsson, C.; Hellström, S.; Luth, S. *Folding Observed in Paleoproterozoic Supracrustal Rocks in Northern Sweden*; Reports and Bulletins; Geological Survey of Sweden: Uppsala, Sweden, 2018; pp. 205–257.
50. Luth, S.; Jönberger, J.; Grigull, S. *The Vakko and Kovo Greenstone Belts: Integrating Structural Geological Mapping and Geophysical Modelling*; Reports and Bulletins; Geological Survey of Sweden: Uppsala, Sweden, 2018; pp. 287–310.
51. Skyttä, P.; Bauer, T.E.; Tavakoli, S.; Hermansson, T.; Andersson, J.; Weihed, P. Pre-1.87Ga development of crustal domains overprinted by 1.87Ga transpression in the Palaeoproterozoic Skellefte district, Sweden. *Precambrian Res.* **2012**, *206–207*, 109–136. [[CrossRef](#)]
52. Skyttä, P.; Määttä, M.; Palsatech, O.Y.; Piippo, S.; Kara, J.; Käpyaho, A.; Heilimo, E.; O’Brien, H. Constraints over the age of magmatism and subsequent deformation for the Neoproterozoic Kukkola Gneiss Complex, northern Fennoscandia. *Bull. Geol. Soc. Finl.* **2020**, *92*, 19–38. [[CrossRef](#)]
53. Sarlus, Z.; Andersson, U.B.; Bauer, T.E.; Wanhainen, C.; Martinsson, O.; Nordin, R.; Andersson, J.B.H. Timing of plutonism in the Gällivare area: Implications for Proterozoic crustal development in the northern Norrbotten ore district, Sweden. *Geol. Mag.* **2018**, *155*, 1351–1376. [[CrossRef](#)]
54. Öhlander, B.; Skiöld, T. Diversity of 1.8 Ga potassic granitoids along the edge of the Archaean craton in northern Scandinavia: A result of melt formation at various depths and from various sources. *Lithos* **1994**, *33*, 265–283. [[CrossRef](#)]
55. Högdahl, K.; Andersson, U.B.; Eklund, O. *The Transscandinavian Igneous Belt (TIB) in Sweden: A Review of Its Character and Evolution*; Högdahl, K., Andersson, U.B., Eklund, O., Eds.; Special paper / geological Survey of Finland; Geological Survey of Finland: Espoo, Finland, 2004; ISBN 978-951-690-889-5.

56. Martinsson, O.; Bergman, S.; Persson, P.-O.; Schöberg, H.; Billström, K.; Shumlyansky, L. *Stratigraphy and Ages of Palaeoproterozoic Metavolcanic and Metasedimentary Rocks at Käymäjärvi, Northern Sweden*; Reports and Bulletins; Geological Survey of Sweden: Uppsala, Sweden, 2018; pp. 79–105.
57. Blomgren, H. U-Pb Dating of Monazites from the Kiirunavaara and Rektorn Ore Deposits. Master's Thesis, University of Gothenburg, Gothenburg, Sweden, 2015.
58. Westhues, A.; Hanchar, J.M.; Voisey, C.R.; Whitehouse, M.J.; Rossmann, G.R.; Wirth, R. Tracing the fluid evolution of the Kiruna iron oxide apatite deposits using zircon, monazite, and whole rock trace elements and isotopic studies. *Chem. Geol.* **2017**, *466*, 303–322. [[CrossRef](#)]
59. Romer, R.L. U-Pb systematics of stilbite-bearing low-temperature mineral assemblages from the Malmberget iron ore, northern Sweden. *Geochem. Cosmochim. Acta* **1996**, *60*, 1951–1961. [[CrossRef](#)]
60. Lundbohm, H.J. Sketch of the Geology of the Kiruna district. *Geol. Föreningen I Stockh. Förhandlingar* **1910**, *32*, 751–788. [[CrossRef](#)]
61. Frietsch, R. *Petrology of the Kurravaara Area Northeast of Kiruna northern Sweden*; Serie C; Sveriges Geologiska Undersökning: Uppsala, Sweden, 1979; p. 85.
62. Martinsson, O.; Perdahl, J.-A.; Bergman, J. *Greenstone and Porphyry Hosted Ore Deposits in Northern Norrbotten*; Research Programme Ore Geology Related to Prospecting; Nutek: Uppsala, Sweden, 1993; p. 78.
63. Welin, E. The depositional evolution of the Svecofennian supracrustal sequence in Finland and Sweden. *Precambrian Res.* **1987**, *35*, 95–113. [[CrossRef](#)]
64. Offerberg, J. *Berggrundsgeologiska och Flygmagnetiska Kartbladen, Kiruna NV, NO, SV, SO*; Af 1–4; Sveriges Geologiska Undersökning (map): Stockholm, Sweden, 1967; 147p.
65. Witschard, F. The geological and tectonic evolution of the Precambrian of northern Sweden—A case for basement reactivation? *Precambrian Res.* **1984**, *23*, 273–315. [[CrossRef](#)]
66. Billström, K.; Evins, P.; Martinsson, O.; Jeon, H.; Weihed, P. Conflicting zircon vs. titanite U-Pb age systematics and the deposition of the host volcanic sequence to Kiruna-type and IOCG deposits in northern Sweden, Fennoscandian shield. *Precambrian Res.* **2019**, *321*, 123–133. [[CrossRef](#)]
67. Geijer, P.; Ödman, O. *The Emplacement of the Kiruna Iron Ores and Related Deposits*; Serie C; Sveriges Geologiska Undersökning: Stockholm, Sweden, 1974; pp. 1–49.
68. O'Farrelly, K.S. A Stable Isotopic Investigation of the Origin and Evolution of the Kiirunavaara Iron Ore Mine, Northern Sweden. Ph.D. Thesis, University of Wales, College of Cardiff, Cardiff, UK, 1990.
69. Geijer, P. *Geology of the Kiruna District 2: Igneous Rocks and Iron Ores of Kiirunavaara, Luossavaara and Tuolluvaara*; Scientific and practical researches in Lapland arranged by Luossavaara-Kiirunavaara Aktibolag: Stockholm, Sweden, 1910; p. 278.
70. Wright, S. Early Proterozoic Deformational History of the Kiruna District, Northern Sweden. Ph.D. Thesis, University of Minnesota, Minneapolis, MN, USA, 1988.
71. Parák, T. Kiruna iron ores are not “intrusive-magmatic ores of the Kiruna type”. *Econ. Geol.* **1975**, *70*, 1242–1258. [[CrossRef](#)]
72. Westhues, A.; Hanchar, J.M.; LeMessurier, M.J.; Whitehouse, M.J. Evidence for hydrothermal alteration and source regions for the Kiruna iron oxide-apatite ore (northern Sweden) from zircon Hf and O isotopes. *Geology* **2017**, *45*, 571–574. [[CrossRef](#)]
73. Martinsson, O.; Hallberg, A.; Söderholm, K.; Billström, K. Pahtohavare—An epigenetic Cu-Au deposit in the Paleoproterozoic Kiruna Greenstones (Paper III). In *Tectonic Setting and Metallogeny of the Kiruna Greenstones (Ph.D. Thesis)*; Martinsson, O., Ed.; Luleå University of Technology: Luleå, Sweden, 1997; p. 37.
74. Rudashevsky, N.S.; Rudashevsky, V.N. Device for Separation of Solid Particles. Russian Patent #2281808, 27 December 2007.
75. Wiedenbeck, M.; Allé, P.; Corfu, F.; Griffin, W.L.; Meier, M.; Oberli, F.; Quadt, A.V.; Roddick, J.C.; Spiegel, W. Three natural zircon standards for U-Th-Pb, Lu-Hf, trace element and REE analyses. *Geostand. Geoanalytical Res.* **1995**, *19*, 1–23. [[CrossRef](#)]
76. Nasdala, L.; Hofmeister, W.; Norberg, N.; Martinson, J.M.; Corfu, F.; Dörr, W.; Kamo, S.L.; Kennedy, A.K.; Kronz, A.; Reiners, P.W.; et al. Zircon M257—A Homogeneous Natural Reference Material for the Ion Microprobe U-Pb Analysis of Zircon. *Geostand. Geoanalytical Res.* **2008**, *32*, 247–265. [[CrossRef](#)]
77. Whitehouse, M.J.; Kamber, B.S. Assigning Dates to Thin Gneissic Veins in High-Grade Metamorphic Terranes: A Cautionary Tale from Akilia, Southwest Greenland. *J. Petrol.* **2005**, *46*, 291–318. [[CrossRef](#)]
78. Jeon, H.; Whitehouse, M.J. A Critical Evaluation of U-Pb Calibration Schemes Used in SIMS Zircon Geochronology. *Geostand. Geoanal. Res.* **2015**, *39*, 443–452. [[CrossRef](#)]
79. Stern, R.A.; Amelin, Y. Assessment of errors in SIMS zircon U-Pb geochronology using a natural zircon standard and NIST SRM 610 glass. *Chem. Geol.* **2003**, *197*, 111–142. [[CrossRef](#)]
80. Shimizu, N.; Hart, S.R. Applications of the Ion Microprobe to Geochemistry and Cosmochemistry. *Annu. Rev. Earth Planet. Sci.* **1982**, *10*, 483–526. [[CrossRef](#)]
81. Stacey, J.S.; Kramers, J.D. Approximation of terrestrial lead isotope evolution by a two-stage model. *Earth Planet. Sci. Lett.* **1975**, *26*, 207–221. [[CrossRef](#)]
82. Whitehouse, M.J.; Pease, V.; Al-Khirbash, S. Neoproterozoic crustal growth at the margin of the East Gondwana continent—Age and isotopic constraints from the easternmost inliers of Oman. *Int. Geol. Rev.* **2016**, *58*, 2046–2064. [[CrossRef](#)]
83. Ludwig, K.R. *PBDAT for MS-DOS; a Computer Program for IBM-PC Compatibles for Processing Raw Pb-U-Th Isotope Data*; Version 1.00 a; US Geological Survey: Reston, VA, USA, 1988; p. 37.

84. Steiger, R.H.; Jäger, E. Subcommission on geochronology: Convention on the use of decay constants in geo- and cosmochronology. *Earth Planet. Sci. Lett.* **1977**, *36*, 359–362. [[CrossRef](#)]
85. Holland, H.D.; Gottfried, D. The effect of nuclear radiation on the structure of zircon. *Acta Cryst.* **1955**, *8*, 291–300. [[CrossRef](#)]
86. Corfu, F. Atlas of Zircon Textures. *Rev. Mineral. Geochem.* **2003**, *53*, 469–500. [[CrossRef](#)]
87. Skiöld, T.; Page, R.W. SHRIMP and isotope dilution zircon ages on Archaean basement-cover rocks in northern Sweden. *Nord. Geol. Vintermøde Aarhus* **1998**, 273.
88. Hughes, C.J. Spilites, keratophyres, and the igneous spectrum. *Geol. Mag.* **1972**, *109*, 513–527. [[CrossRef](#)]
89. de la Roche, H.; Leterrier, J.; Grandclaude, P.; Marchal, M. A classification of volcanic and plutonic rocks using R1 R2-diagram and major-element analyses—Its relationships with current nomenclature. *Chem. Geol.* **1980**, *29*, 183–210. [[CrossRef](#)]
90. Pearce, J.A.; Harris, N.B.W.; Tindle, A.G. Trace Element Discrimination Diagrams for the Tectonic Interpretation of Granitic Rocks. *J. Petrol.* **1984**, *25*, 956–983. [[CrossRef](#)]
91. Schandl, E.S.; Gorton, M.P. Application of high field strength elements to discriminate tectonic settings in VMS environments. *Econ. Geol.* **2002**, *97*, 629–642. [[CrossRef](#)]
92. Sun, S.-S.; McDonough, W.F. Chemical and isotopic systematics of oceanic basalts: Implications for mantle composition and processes. *Geol. Soc. Lond. Spec. Publ.* **1989**, *42*, 313–345. [[CrossRef](#)]
93. Martinsson, O.; Perdahl, J.-A. Paleoproterozoic extensional and compressional magmatism in northern Norrbotten, northern Sweden (Paper II). In *Svecofennian Volcanism in Northernmost Sweden (Ph.D. Thesis)*; Perdahl, J.-A., Ed.; Luleå University of Technology: Luleå, Sweden, 1995; p. 161.
94. Middlemost, E.A.K. Naming materials in the magma/igneous rock system. *Earth Sci. Rev.* **1994**, *37*, 215–224. [[CrossRef](#)]
95. Troll, V.R.; Weis, F.A.; Jonsson, E.; Andersson, U.B.; Majidi, S.A.; Högdahl, K.; Harris, C.; Millet, M.-A.; Chinnasamy, S.S.; Kooijman, E.; et al. Global Fe–O isotope correlation reveals magmatic origin of Kiruna-type apatite-iron-oxide ores. *Nat. Commun.* **2019**, *10*, 1712. [[CrossRef](#)]
96. Parák, T. Phosphorus in different types of ore, sulfides in the iron deposits, and the type and origin of ores at Kiruna. *Econ. Geol.* **1985**, *80*, 646–665. [[CrossRef](#)]
97. Sarlus, Z. Timing and Origin of Igneous Rocks in the Gällivare area, Northern Sweden. Ph.D. Thesis, Luleå Tekniska Universitet, Luleå, Sweden, 2018.
98. Naslund, H.; Mungall, J.; Henríquez, F.; Nyström, J.; Lledó, H.; Lester, G.; Aquirre, R. *Melt Inclusions in Silicate Lavas and Iron-Oxide Tephra of the El Lago Volcano, Chile*; Facultad de ciencias físicas y matemáticas universidad de Chile: Santiago, Chile, 2009; p. 4.
99. Bain, W.M.; Steele-MacInnis, M.; Tornos, F.; Hanchar, J.M.; Creaser, E.C.; Pietruszka, D.K. Evidence for iron-rich sulfate melt during magnetite(-apatite) mineralization at El Lago, Chile. *Geology* **2021**, *49*, 1044–1048. [[CrossRef](#)]
100. BABEL Working Group. Evidence for early Proterozoic plate tectonics from seismic reflection profiles in the Baltic shield. *Nature* **1990**, *348*, 34–38. [[CrossRef](#)]
101. Martinsson, O. Genesis of the Per Geijer Apatite Iron Ores, Kiruna Area, Northern Sweden. In Proceedings of the SGA Biennial Meeting, Nancy, France, 23–27 August 2015; Abstract volume, pp. 23–27.
102. Perdahl, J.-A.; Frietsch, R. Petrochemical and petrological characteristics of 1.9 Ga old volcanics in northern Sweden. *Precambrian Res.* **1993**, *64*, 239–252. [[CrossRef](#)]
103. Tavakoli, S.; Sarlus, Z.; Kronsell, I.; Bauer, T.E. 2.5D geophysical model of the Gällivare mining area: An integrated study to model the top 4 km of the subsurface and guide for future exploration activities. *Geophys. Prospect.* **2021**, *69*, 821–841. [[CrossRef](#)]